Transient behavior in quasi-atomic layer etching of silicon dioxide and silicon nitride in fluorocarbon plasmas

Chad M. Huard,[1,a),b)] Saravanapriyan Sriraman,[2,c)] Alex Paterson,[2,d)] and Mark J. Kushner[1,e)]

[1]*Department of Electrical Engineering and Computer Science, University of Michigan, 1301 Beal Ave., Ann Arbor, Michigan 48109-2122*
[2]*Lam Research Corp., 4650 Cushing Parkway, Fremont, California 94538*

The mechanism for atomic layer etching (ALE) typically consists of two sequential self-limited half-reactions—passivation and ion bombardment—which provide unique control over the process. Some of the possible benefits of this control include increased selectivity, reduced plasma induced damage, improved uniformity and aspect ratio independence. To achieve the greatest benefit from ALE, both half-reactions should be fully self-limited. In the experimental demonstration of ALE of SiO_2 using fluorocarbon plasmas, the passivation phase typically consists of deposition of fluoropolymer on the SiO_2 surface. This passivation step is not a self-limited reaction as the final polymer thickness depends on the passivation time. In this paper, results are presented from a computational investigation of the ALE of SiO_2 and Si_3N_4 focusing on the implications of this nonself-limited passivation phase. The polymer overlayer was found to be critically important to the ALE performance, providing the main mechanism for selectivity between SiO_2 and Si_3N_4. The polymer overlayer acts as a fuel for etching SiO_2, which couples the etch depth per ALE cycle to the passivation time. Due to the inherently pulsed nature of the ALE mechanism, the polymer overlayer requires a finite number of cycles to reach a pulsed periodic steady-state thickness. Since the thickness of the polymer overlayer largely determines selectivity between SiO_2 and Si_3N_4, the initial formation of an overlayer results in a transient period at the beginning of etching where high selectivity may not be achieved. For the etching of thin films, or applications which require very high selectivity, this transient etching period may be a limiting factor. Results are also presented using ALE to etch high aspect ratio self-aligned contacts which could not be cleared using continuous plasma etching with similar ion energies and flux ratios. *Published by the AVS.* https://doi.org/10.1116/1.5049225

I. INTRODUCTION

Plasma based atomic layer etching (ALE) is a technique which can provide significant advantages over conventional etching.[1] The benefits of ALE arise from separating the etch mechanism into two half-reactions. In ideal ALE, each of these half-reactions is fully self-limited and would produce no continuous etching if individually employed. Only by cycling between the half-reactions does etching occur. The most basic ALE process is separated into a passivation phase and an etching phase. In plasma based ALE, the passivation and etching phases occur in sequentially applied plasmas, typically produced by exchanging gases. Passivation, which lowers the chemical sputtering threshold energy, is typically accomplished by diffusive transport of neutral radical species through the feature to the etch front. Etching is then accomplished using ion bombardment, in which low energy ions preferentially etch the passivated species after anisotropically transporting through the feature. This separation of passivation and ion bombardment enables the fluxes of radicals and ions to be separately optimized despite their different transport methods. The use of self-limited reactions for each of these phases allows for over-exposure to increase uniformity on the macroscale (wafer) and microscale. An important example of microscale nonuniformity that can be addressed by ALE is aspect ratio dependent etching (ARDE).[2] ALE also offers a method for improving selectivity and reducing damage.

Plasma based ALE processes have been developed for several materials. In particular, materials which can be passivated by halogen radicals result in strong self-limiting behavior.[3] Halogen passivation using, for example, a Cl_2 or Br_2 containing plasma is ideal for ALE due to the covalent interaction between the halogen radicals produced in the plasma and the underlying material which results in rapidly producing a tightly bound passivation layer. Once the top surface of the underlying material is fully passivated, that is saturated, the inability for thermal halogen radicals to penetrate through the passivation layer prevents underlying layers from reacting with the halogen. The strength of the halogen bond can weaken the binding energy of the surface atoms with the underlying lattice, creating an energy window where incoming ions can sputter passivated surface atoms, but do not have enough energy to remove unpassivated bare material sites. This energy window enables a carefully controlled ion energy distribution (IED) of the ion flux to preferentially remove the passivated surface layer, a process that

a)Electronic mail: chuard@umich.edu
b)Present address: KLA-Tencor Corp., 8834 N. Capital of Texas HW, Suite 301, Austin, TX 78759; electronic mail: Chad.Huard@kla-tencor.com
c)Electronic mail: Saravanapriyan.Sriraman@lamresearch.com
d)Electronic mail: Alex.Paterson@lamresearch.com
e)Author to whom correspondence should be addressed: mjkush@umich.edu

terminates when that layer is removed, resulting in self-limiting behavior in the ion bombardment phase.

Atomic layer etching of SiO$_2$ has been experimentally demonstrated using fluorocarbon radical species for surface passivation instead of halogen passivation.[4] The carbon is required to remove the oxygen of the SiO$_2$ due to the lack of a strong fluorine–oxygen bond. Unfortunately, this passivation process is not self-limited as C–C bonds allow for the accumulation of a fluorocarbon polymer on the surface of the SiO$_2$. For the conditions of interest, this fluorocarbon polymer deposition is a continuous process which does not saturate in time. The end result is a fluorocarbon polymer overlayer thickness that depends on the total fluence of fluorocarbon radicals during the passivation phase, which in turn depends on the duration of the passivation phase and, locally, on the uniformity of the passivation fluxes in the feature. These dependencies could diminish some of the benefits of ALE of SiO$_2$.

Experiments have shown that during continuous fluorocarbon plasma etching of dielectrics, a steady-state thickness of polymer is formed.[5] The thickness of the polymer overlayer is critical to the fluorocarbon etching mechanism as it mediates the flux of plasma produced reactive species and ion energy from the plasma to the etch interface. The difference in polymer overlayer thickness between SiO$_2$ and Si$_3$N$_4$ is a dominant factor in achieving selectivity of etching SiO$_2$ over Si$_3$N$_4$, a requirement for several processes used in semiconductor fabrication.[6]

There are several factors which affect the steady-state polymer thickness on dielectrics etched in fluorocarbon plasmas. To achieve a steady-state thickness, polymer deposition must be balanced by polymer loss. It is clear from experimental data that a fairly wide range of plasma conditions will produce steady-state polymer thicknesses.[6] For this to be possible, either the deposition rate or loss term must depend on polymer thickness, such as

$$\frac{dp}{dt} = D - Sp = 0, \tag{1}$$

where p is the polymer thickness (cm), D is the polymer deposition rate (cm s^{-1}), and Sp is the polymer etch rate. In the steady state, $p = D/S$. In this simple model, the deposition rate is

$$D = \frac{a_p \phi_p}{\rho}, \tag{2}$$

where ϕ_p is the incident flux of polymerizing species, a_p is the probability for depositing on the underlying polymer, and ρ is the volumetric number density of the film. While the polymer etch rate in the physical system may not be linearly dependent on polymer thickness, as proposed in Eq. (1), there must be some dependency on polymer thickness or there would only be a single D/S ratio which would produce steady-state polymer thickness, which is not the experimental observation. The polymer etch rate, Sp (cm s^{-1}), is

conceptually given by

$$S = a_e \phi_e D, \tag{3}$$

where ϕ_e is the incident flux of polymer removing (or etching) species, a_e is the probability for etching the polymer, and D is the diffusivity of the etching species in the polymer film. This simple analysis implies that the deposition of polymer is a surface dominated process, depending on the exposed area of the feature, while polymer etching is a volumetric process, depending on the thickness of the polymer. This is a physically consistent picture for producing a steady-state polymer thickness provided that the etching species is not significantly depleted in transporting through the polymer layer. In plasma etching of, for example, SiO$_2$ in fluorocarbon plasmas, polymer deposition occurs dominantly by incorporation of radicals (e.g., CF, CF$_2$, CF$_3$) into the outermost surface of the polymer. Polymer etching, on the other hand, occurs predominantly due to thermal reactions with reactive radicals (e.g., F, O), which can diffuse through the bulk of the polymer, resulting in a volumetric process.[7]

These deposition and loss mechanisms depend only on plasma properties, and in principle should be identical on all materials exposed to the same plasma provided the surface is covered by at least one monolayer of polymer. The difference between steady-state polymer thickness on different materials is then due to different rates of consumption of polymer at the etching interface between the polymer and the underlying material. These differences in polymer consumption result from the different stoichiometries of producing etch products for each material. When etching SiO$_2$, silicon sites are dominantly removed as SiF$_x$ products, while oxygen is removed from the surface mainly as CO or COF$_2$.[8] Therefore, for each Si atom removed, the etch process will consume two carbon atoms from the polymer overlayer. On bare silicon, this consumption of carbon by the formation of C–O bonds does not take place, resulting in a less polymer loss compared to SiO$_2$ which, in turn, results in a thicker polymer layer on silicon. The interface reactions of polymer on Si$_3$N$_4$ (forming, for example, etch product CNF) removes carbon at a rate that is intermediate between SiO$_2$ and silicon, producing a polymer layer that is also intermediate in thickness.[6]

The importance of controlling the polymer thickness during ALE to achieve selectivity of SiO$_2$ to Si$_3$N$_4$, or Si$_3$N$_4$ to SiO$_2$ has been experimentally investigated by Li *et al.*[9] They found that selectivity could be controlled by combinations of polymer thickness and ion energy, the latter capitalizing on the different thresholds for activation of SiO$_2$ and Si$_3$N$_4$ etching. Thicker polymer films and higher ion energies favored selectivity of SiO$_2$ over Si$_3$N$_4$. Thinner polymer films and lower ion energies favored selectivity of Si$_3$N$_4$ over SiO$_2$.

Kinetic models of the SiO$_2$ etching process have been developed which can describe the polymer coverage and etch rates for various plasma conditions.[10,11] Such models allow for the etch yield, as well as source and loss terms for polymer deposition/etching, to depend on the polymer

thickness, as has been seen experimentally. While kinetic models can accurately describe the etching mechanisms for a single set of plasma conditions, these conditions can significantly vary within a typical etch feature, which in turn requires feature scale modeling to resolve.

To predict the evolution of an etch feature, a model should include transport of reactive species through the feature and position dependent etch rates. Current feature scale models typically rely on either the level-set technique or cell based methods. Level-set methods are used to track the propagation of the etch or deposition front (that is, the top surface of the material) in the presence of a locally varying forcing function.[12] In plasma etch modeling, the local rate of etch front propagation typically depends on the ratio of neutral to ion fluxes. This technique has been used to model the etching of silicon with a pulsed Bosch process using two simultaneously propagating level sets to track the passivation front separately from the underlying silicon.[13] Etching of SiO$_2$ in fluorocarbon plasma was modeled by Shimada *et al.* using a single level set to track the etch front propagation.[14] In this case, the polymer thickness was tracked separately for each point on the etch surface and etch rate depended on the local polymer thickness.

Cellular models divide the simulation domain into a computational grid in which each cell or voxel represents the material of that region of space. Individual computational cells can represent a single material or be fractionally filled by different material species which aids in smoothing statistical noise.[15] Fractional filling of cells can also be used to resolve some of the kinetics of the mixing layer. The ratio and number of these species in a single cell then determine the reaction probability for incoming pseudoparticles representing the plasma produced fluxes. This technique was used by Guo *et al.* to study Cl$_2$ plasma etching of silicon and Ar/C$_4$F$_8$ plasma etching of SiO$_2$.[16,17] Cellular models have also been employed to study oxide etching in three–dimensional (3D) features.[18]

Cellular models have also been used to represent ion implantation into the substrate. For example, Osano and Ono tracked the implantation of Cl$^+$ and O$^+$ ions into silicon using Monte Carlo techniques.[19–21] The distribution of implanted reactants was then used to obtain chemical sputtering probabilities which depended on the local density of implanted species. Takagi *et al.* used a more continuous approximation to study the effect of ion energy loss in a polymer layer while etching SiO$_2$.[22,23] In this model, the polymer thickness was determined by local (position dependent) radical fluxes. The polymer thickness was then used to calculate a local etch rate based on an analytical slowing of ions in the polymer. Kuboi *et al.* developed a 3D cellular voxel model to investigate damage occurring during plasma etching of Si$_3$N$_4$.[24] The model accurately predicted the experimentally measured polymer thickness on Si, SiO$_2$, and SiN as a function of fluorocarbon gas flow rate, and selectivity of SiO$_2$ over SiN.

In this paper, a feature scale, cellular voxel based model is presented that can accurately describe the steady-state polymer overlayer formation on Si, SiO$_2$, and Si$_3$N$_4$ in fluorocarbon plasmas. The model was applied to the investigation of ALE and selective etching of SiO$_2$ and Si$_3$N$_4$, This model represents energy and mass transport to the etch interface through the overlayer using Monte Carlo techniques. Neutral and ion energy activated processes can occur at the etch front, with reactants and products being transported through the overlayer.

The feature scale model and the reactor scale model used to generate plasma produced fluxes to the surface are described in Sec. II. The reaction mechanism for the fluorocarbon plasma etching process is described in Sec. III. An inductively coupled plasma (ICP) sustained in Ar/C$_4$F$_8$ is described in Sec. IV, along with validation of continuous etch behavior. This model was then used to investigate the impact of nonself-limited polymer deposition on ALE, as described in Sec. V. In Sec. VI, results of using ALE to clear high aspect ratio self-aligned contact (SAC) features are presented. A discussion of the importance of the polymer processes on ALE is presented in Sec. VII. These results indicate that the etch per cycle (EPC) of ALE depends on the polymer layer thickness and therefore on the passivation time. These findings indicate that ALE can be used to carefully control polymerization, clearing features which would be difficult with continuous etching with very high selectivity.

II. DESCRIPTION OF THE MODELS

Modeling of the reactor scale plasma conditions in an ICP etching chamber was performed using the Hybrid Plasma Equipment Model (HPEM).[25] The HPEM solves for relevant, spatially dependent, plasma properties using a hybrid time slicing technique with each physical process being calculated with a frequency related to the characteristic time of that process. In this particular implementation, harmonic electromagnetic fields due to the radio frequency (RF) current passing through a flat coil antenna were calculated by solving the frequency domain wave equation. Boltzmann's equation for the spatially dependent electron energy distribution in these fields was solved using a kinetic Monte Carlo technique. The resulting distributions were used to calculate electron impact source functions based on energy dependent cross sections. The source and loss terms from the electron impact processes were then used in a fluid model, which solves continuity, momentum, and energy equations for ion and neutral gas species. The resulting spatially resolved species densities are used to calculate positional charge density in the gas phase and on surfaces. Poisson's equation is then solved for the electrostatic potential, and the entire process is repeated until the system reaches a converged self-consistent solution. Details of the gas phase reaction mechanism used for Ar/C$_4$F$_8$ plasma chemistry were previously described by Vasenkov *et al.*[26]

The resulting source functions for ions and neutral radicals and time varying electromagnetic and electrostatic fields are then used to perform a Monte Carlo particle simulation to track the trajectories of ions and neutrals originating in the plasma, traversing the plasma sheath and striking the wafer. This process results in the flux of each reactive species, as

well as the energy and angular distributions (EADs) for ions and neutrals as they arrive at the wafer.

The predictions for on-wafer features were obtained using the Monte Carlo Feature Profile Model (MCFPM).[27] The MCFPM uses a cellular model; discretizing the feature into a 3D cubic mesh of computational cells, each with a single material identity. Pseudoparticles representing the gas phase reactive species incident from the plasma are chosen with properties selected using Monte Carlo techniques from the fluxes and EADs generated by the HPEM. These pseudoparticles are tracked through space until intersecting a solid mesh cell. Reactions between solid and gas species are defined in a user supplied reaction mechanism and can include chemical reactions (which change the material identity of the reacting solid cell), etching reactions (which remove the solid cell from the mesh), and deposition reactions (which deposit a new solid cell on top of the original cell).

While many of the results presented here are for features which are effectively two-dimensional (2D) (e.g., infinite trench) or one-dimensional (e.g., unpatterned blanket etch), all simulations were performed in 3D using the same reaction mechanism to maintain consistency. For example, a 2D trench was modeled in 3D as an initially uniform 2D feature having a finite depth, typically 10–20 computational cells, using periodic boundary conditions. In a purely 2D representation, roughness or deposition on a surface is manifested in the model as an infinite line of such roughness or deposition, which may over-emphasize effects such as twisting. By having some finite 3D depth to a 2D feature, the roughness is more accurately represented.

In polymer mediated etching of dielectrics, several classes of reactions occur of gas phase species with the overlying polymer, and at the polymer-substrate interface. To include such reactions, updates were made to the MCFPM. To capture the transport of energy and reactive species through the polymer capping layer, 3D ion implantation (and the resulting mixing) and neutral diffusion through solids were added to the model. The 3D diffusion of surface adsorbed species before chemisorption was also added to aid in modeling the polymer growth during fluorocarbon plasma processing. Both ion implant/mixing[28] and surface diffusion[29] were previously included in the MCFPM in various forms. However, the 3D models implemented here significantly differ in implementation and physical intent. Due to the significant changes to the MCFPM algorithms, a fairly complete review of the model will be given here.

In the MCFPM, the simulation time is calculated by assigning each incoming pseudo-particle a time weight of

$$\Delta t = \frac{N_s}{\Gamma_t A},\tag{4}$$

where N_s is the average number of atoms per solid computational cell (a user input), Γ_t is the total flux of all gas phase species entering the feature (cm^{-2} s^{-1}), and A is the area through which the flux is launched into the computational domain. Scaling the time weighting of each pseudo-particle

by N_s in Eq. (4) is required to enable gas phase particles to react stoichiometrically with solid cells having nonunity numbers of atoms per cell.

In a pulsed plasma simulation, such as for ALE, the MCFPM uses the total fluxes of each subcycle (m) to calculate the time per particle for that particular subcycle, Δt_m. The length of the subcycles is defined by the user in seconds. The model converts the user defined subcycle time into a number of particles using the Δt_m of that subcycle. This results in each subcycle having the same number of particles per subcycle from period to period. Physically, the number of particles per subcycle should be Poisson distributed, but in the case where the number of particles is large this distribution will have a very little effect. The shortest subcycle used in the simulations discussed here used 2×10^4 particles, resulting in a deviation of less than 1% in the number of particles in each subcycle from pulse to pulse when using Poisson statistics. This pulse-to-pulse variation is not expected to significantly affect the results, and the constant Δt for each particle can be assumed. Species having low fluxes are chosen at random by Monte Carlo techniques (described shortly). In this way, the number of a given low flux species released in a given cycle will be Poisson distributed, despite the total number of particles in that cycle being fixed.

The trajectories of the incoming pseudoparticles are advanced in three dimensions through continuous space until they impact a solid mesh cell. When a pseudo-particle strikes a solid surface, a reaction is chosen from a user defined reaction mechanism. This mechanism can include reactions with both energy and angular dependencies. Based on this reaction mechanism, particle collisions can result in a reflection of the incoming particle without changing the material cell properties. After a particle collides with a surface, any resulting particles emitted into the gas phase—including etch products and/or the original particle—are tracked in a similar manner as the initially launched particle until the next collision with a surface. This process is repeated for each particle until that particle (and the gas phase particles it generates) is removed by reacting with a surface, or the particle leaves the computational domain by scattering out of the top of the domain.

Pseudoparticles are initialized such that their fluxes, as well as energy and angle distributions, statistically match the distributions obtained from reactor scale modeling. This is a two-step process. The cumulative distribution function, f_{ci}, of the flux of individual neutral and charges species incident onto the surface is defined as

$$f_{ci} = \sum_1^i f_i / \sum_1^N f_i,\tag{5}$$

where f_i is the flux of species i for N species. The species selected for launching toward the surface is that satisfying

$$f_{c,i-1} < r \le f_{c,i},\tag{6}$$

where r is a random number evenly distributed on [0,1]. A

similar cumulative distribution function is constructed for the EAD of each particle. Choice of another random number then defines the energy and angle with respect to the vertical with which the particle is launched toward the surface. The spatial location is randomly selected in the plane perpendicular to the normal, requiring an additional two random numbers. Particles are launched from 3 to 10 nm above the top surface of the material mesh.

Particles are advanced in time through 3D continuous space according to a first order explicit discretization of Newton's equations:

$$\mathbf{v}_\tau = \mathbf{v}_{\tau-1} + \frac{q\mathbf{E}}{m}\Delta\tau, \tag{7}$$

and

$$\mathbf{r}_\tau = \mathbf{r}_{\tau-1} + \mathbf{v}_\tau\Delta\tau, \tag{8}$$

where $\mathbf{v}_\tau$ is the velocity at particle time τ, $\mathbf{r}_\tau$ is the position, q is the particle charge, m is the particle mass, and $\mathbf{E}$ is the electric field. In this study, electric potentials due to charging were not calculated so that the electric field is zero. The variable τ is used to denote particle time to emphasize the difference between the particle time step $\Delta\tau$ and the simulation time step Δt. As previously discussed, Δt is the period (in simulation time) between particles impinging on the simulation domain. $\Delta\tau$ is chosen to be the time required to cross at most two computational cells and so depends on the speed of the particle. This choice of $\Delta\tau$ allows particles to occasionally pass through very small obstructions in the particle trajectory, providing a type of real-time smoothing of the surface roughness. The behavior of each of those particles is considered instantaneous in simulation time.

As the particle is tracked through continuous space, it is mapped onto the computational mesh of materials using

$$i = \lfloor r_x \Delta x \rfloor + 1, \tag{9a}$$

$$j = \lfloor r_y \Delta y \rfloor + 1, \tag{9b}$$

$$k = \lfloor r_k \Delta z \rfloor + 1, \tag{9c}$$

where $\lfloor x \rfloor$ is the floor function of x and r_x is the component of the current position vector $\mathbf{r}$ in the $\hat{e}_x$ direction. The particle is mapped onto cell $\mathbf{M}_{i,j,k}$ of the 3D matrix, $\mathbf{M}$, which represents the material of that region of space. The use of the floor function in this mapping guarantees that the lower boundary and upper boundary of each index are handled symmetrically.

At each step in particle time, the material matrix, $\mathbf{M}$, is checked to determine when a particle enters a solid material. The particle is assumed to have a finite (user defined) size, Δx_p, occupying a cubic volume $\pm\Delta x_p$ around the current position $\mathbf{r}$ in each dimension. A collision with the material matrix is only considered fully resolved when a single point

in the seven-point molecule formed by the current position and points located $\pm\Delta x_p$ in each cardinal direction from the current position maps to a mesh cell which is occupied by a solid material. If more than one point in this set maps to a cell which is occupied by a solid material, the particle is returned to its previous position and the propagation time step, $\Delta\tau$, cut in half. This process is repeated until only a single point maps to an occupied cell, at which time that cell is considered to be the impact location.

When a particle collides with the solid material, the surface normal of the profile at the collision point is calculated. This is accomplished by fitting a plane to nearby surface sites and using the normal of this plane as the surface normal. The process begins by finding all surface sites within a user defined search distance, which is ±1.2 nm in this work. As the surface is approximated with a linear function, increasing this search distance works to average local fluctuations and smooth the surface. The size of the search radius also affects the maximum local curvature and therefore the resolution of the feature. Large values of search radius maintain smoother surfaces, but compromise the smallest features which can be represented with the same mesh. Surface sites for fitting the plane are defined as any computational cell with one or more faces exposed to the plasma. The search distance of ±1.2 nm was empirically determined by comparing the predicted surface roughness and sharpness of features with experimental micrographs.

Once all surface sites are found then a plane, defined as $Ax + By + Cz = D$, is fit to the points by finding A, B, C, and D such that they minimize the sum of the squared error,

$$Q = \sum_{i=1}^{m} (Ax_i + By_i + Cz_i - D)^2, \tag{10}$$

where m is the number of surface points within the search region and x_i, y_i, and z_i are the x, y, z locations of the centers of the ith surface point in that set. The derivative of Q with respect to each coefficient has two points where it reaches zero, the best and worst fits. To find the best fit, we solve for the coefficients by setting each derivative to zero,[30]

$$\frac{dQ}{dA} = \sum_{i=1}^{m} 2x_i(Ax_i + By_i + Cz_i - D) = 0,$$

$$\frac{dQ}{dB} = \sum_{i=1}^{m} 2y_i(Ax_i + By_i + Cz_i - D) = 0, \tag{11}$$

$$\frac{dQ}{dC} = \sum_{i=1}^{m} 2z_i(Ax_i + By_i + Cz_i - D) = 0.$$

The value of D can be found as the center of mass of the surface points,

$$D = \frac{A}{m}\sum_{i=1}^{m} x_i + \frac{B}{m}\sum_{i=1}^{m} y_i + \frac{C}{m}\sum_{i=1}^{m} z_i$$

$$= A\bar{x} + B\bar{y} + C\bar{z}. \tag{12}$$

Substituting Eq. (12) back into Eq. (11) results in the system of equations:

$$
\begin{bmatrix}
\sum_{i=1}^{m}(x_i-\bar{x})^2 & \sum_{i=1}^{m}(x_i-\bar{x})(y_i-\bar{y}) & \sum_{i=1}^{m}(x_i-\bar{x})(z_i-\bar{z}) \\
\sum_{i=1}^{m}(x_i-\bar{x})(y_i-\bar{y}) & \sum_{i=1}^{m}(y_i-\bar{y})^2 & \sum_{i=1}^{m}(y_i-\bar{y})(z_i-\bar{z}) \\
\sum_{i=1}^{m}(x_i-\bar{x})(z_i-\bar{z}) & \sum_{i=1}^{m}(y_i-\bar{y})(z_i-\bar{z}) & \sum_{i=1}^{m}(z_i-\bar{z})^2
\end{bmatrix}
\times
\begin{bmatrix} A \\ B \\ C \end{bmatrix}
=
\begin{bmatrix} 0 \\ 0 \\ 0 \end{bmatrix}.
$$

(13)

This system of equations can be solved as an eigenvalue problem by assuming $A^2 + B^2 + C^2 = 1$ (to avoid the trivial solution) and using the Jacobi algorithm.[31] This algorithm returns three eigenvectors and three eigenvalues. The eigenvector corresponding to the smallest eigenvalue is parallel to the unit normal of the profile at the impact site.

Since the algorithm described above only has information about the surface, and not the state of the surrounding solid or gas cells, it is possible that the unit vector returned will be pointing into the solid. To select a normal vector of the surface pointing into the plasma, three points along the given vector are polled in the positive and negative directions. If the point maps to a cell which is occupied by a solid material, it casts a vote against that direction being the surface normal. If the cell is unoccupied (gas), the point casts a vote in favor of that direction being the surface normal. If one direction has more votes for it than the other, it is selected as the surface normal. If the vote is tied, then the sign of the surface normal is selected at random.

When gas particles interact with the solid material, the resulting reflected or reemitted particles have a mechanism dependent velocity distribution. If the particle is energetic, meaning that it has >1 eV translational energy, it has a tendency to specularly reflect from a surface. In the MCFPM, all ions (positive and negative) neutralize when striking surfaces, retaining an energy and angular dependent fraction of their incident energy as a *hot neutral* particle, dispersed in specular and diffusive modes, as described below. All processes involving energetic particles apply equally to energetic ions and hot neutrals.

In a specular reflection, the angle between the incoming particle velocity $\mathbf{v}_i$ and the surface normal vector $\mathbf{n}$ is the same as the angle between the final velocity $\mathbf{v}_f$ and $\mathbf{n}$. The component of the velocity which is tangential to the surface normal does not change during purely specular reflection. The resulting velocity is computed using the vector expression,[32]

$$\hat{\mathbf{v}}_f = 2(\hat{\mathbf{n}} \cdot \hat{\mathbf{v}}_i)\hat{\mathbf{n}} - \hat{\mathbf{v}}_i,$$

(14)

where hatted vectors are the unit direction vectors.

Particles lose energy during the reflection as a function of initial energy and incident angle. Both of these processes scale the reflected energy as

$$\varepsilon_f = \gamma_0 f(\theta) f(\varepsilon_i)\varepsilon_i,$$

(15)

where ε_i is the initial energy, ε_f is the final energy, γ_0 is a user defined maximum fraction for the reflected energy, and θ is the angle between the surface and the incoming velocity. Energy dependent energy loss favors retaining a larger proportion of the initial velocity for more energetic particles. The energy scaling factor, $f(\varepsilon_i)$, is zero for initial energies less than ε_0, unity for initial energies greater than ε_s, and scales linearly between the two user defined energies. The angle dependent energy loss term, $f(\theta)$, is unity for $\theta = 0°$ (grazing incidence) and decreases linearly to zero at a user defined θ_0. In this study, the values of $\gamma_0 = 0.85$, $\varepsilon_0 = 0$ eV, $\varepsilon_s = 50$ eV, and $\theta_0 = 30°$ were used for all simulations. The magnitude of the final velocity is then calculated as

$$\mathbf{v}_f = \sqrt{\frac{2\varepsilon_f}{m}}\hat{\mathbf{v}}_f.$$

(16)

Ions are assumed to be neutralized when striking a surface and—in the absence of an electric field—are not distinguished from the hot neutrals which result from reflections of ions from the surface.[33] For simplicity, we use the term *ion* to denote a hot, nonthermal, particle—the initial ion before striking a surface or the hot neutral after striking a surface. Ions whose energy drops below 1 eV by energy lost through reflections are converted to their thermal neutral counterparts and are then indistinguishable from the incoming neutral flux of that species.

Neutral particles with thermal or near thermal (<1 eV) energies reflect or reemit from surfaces diffusively following a cosine angular distribution.[34,35] This distribution results from the particle being in thermal equilibrium with the surface, allowing the particles to briefly physisorb to the surface before being reemitted into the gas by vibrational processes in the solid, such as phonon scattering. This scattering is performed in the MCFPM by assuming the reemitted particle travels in the direction of the surface normal $\mathbf{n}$, in a local coordinate system ($\hat{e}_x'$, $\hat{e}_y'$, $\hat{e}_z'$) where the $\hat{e}_z'$ axis is aligned with $\mathbf{n}$. Two rotations are then applied, first $\mathbf{R}_1(\theta, \varphi)$ applies a rotation in the local coordinates with polar angle θ and azimuthal angle φ. Next, $\mathbf{R}_2(\alpha, \beta)$ rotates the local coordinate system back to the global ($\hat{e}_x$, $\hat{e}_y$, $\hat{e}_z$) coordinates, using the Euler angles α and β. The α and β angles are calculated as

$$\alpha = \arccos\left(\frac{n_x}{\sqrt{n_x^2+n_y^2}}\right), \beta = \arccos\left(\frac{n_z}{\sqrt{n_x^2+n_y^2+n_z^2}}\right),$$
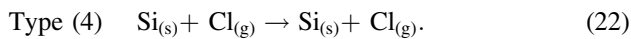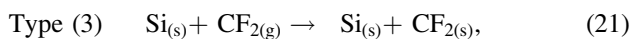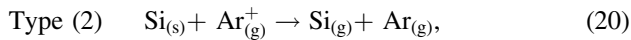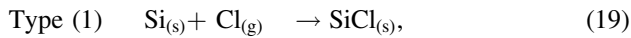
(17)

where n_x is the component of the surface normal in the

global $\hat{e}_x$ direction. The angle α rotates the **n** vector about the $\hat{e}_z$ axis to bring it into the $\hat{e}_x$, $\hat{e}_y$ plane. The angle β rotates the **n** vector again, this time about the $\hat{e}_y$ axis to bring it into alignment with the $\hat{e}_z$ axis. The combined rotation matrix is $\mathbf{R}(\alpha, \beta, \theta, \varphi) = \mathbf{R}_2(\alpha, \beta)\mathbf{R}_1(\theta, \varphi)$. Since the initial velocity is in the $\hat{e}_z'$ direction by construction, the rotation can be applied as

$$
\begin{aligned}
v_x &= v_{th}(\cos(\beta)\cos(\alpha)\sin(\theta)\cos(\varphi) + \cos(\beta)\sin(\alpha)\cos(\theta) \\
&\quad - \sin(\beta)\sin(\theta)\sin(\varphi)), \\
v_y &= v_{th}(\sin(\beta)\cos(\alpha)\sin(\theta)\cos(\varphi) + \sin(\beta)\sin(\alpha)\cos(\theta) \\
&\quad + \cos(\beta)\sin(\theta)\sin(\varphi)), \\
v_z &= v_{th}(-\sin(\alpha)\sin(\theta)\cos(\varphi) + \cos(\alpha)\cos(\theta)),
\end{aligned}
\tag{18}
$$

where v_{th} is the thermal velocity chosen from a Maxwellian energy distribution with a user defined temperature, representing the temperature of the substrate.

Surface reactions occur when a gas phase pseudo-particle interacts with any solid cell in the mesh. These reactions can be (1) chemical reactions that change the material identity, (2) sputtering reactions that convert the cell from a solid material into a gas cell, and (3) deposition reactions that deposit a new solid cell on top of the reaction cell. Each of these reactions is described in a universal reaction format in the MCFPM reaction mechanism. For example,

$$
\text{Type (1)} \quad Si_{(s)} + Cl_{(g)} \rightarrow SiCl_{(s)}, \tag{19}
$$

$$
\text{Type (2)} \quad Si_{(s)} + Ar_{(g)}^+ \rightarrow Si_{(g)} + Ar_{(g)}, \tag{20}
$$

$$
\text{Type (3)} \quad Si_{(s)} + CF_{2(g)} \rightarrow Si_{(s)} + CF_{2(s)}, \tag{21}
$$

$$
\text{Type (4)} \quad Si_{(s)} + Cl_{(g)} \rightarrow Si_{(s)} + Cl_{(g)}. \tag{22}
$$

The reactions can be defined with fixed probabilities, or with energy and angle dependent probabilities. Typically, type (1) and type (3) reactions are defined with fixed probabilities, while type (2) reactions usually have energy and angle dependent reaction probabilities. Type (4) reactions are simply reflections without reaction—the equivalent of an elastic scattering event in the gas phase.

Gas-solid reactions involving thermal reactions are modeled in the MCFPM as having fixed probabilities, which includes most reactions of type (1) and type (3). These thermal reactions in a real etching system would be functions of gas and substrate temperatures. In the MCFPM, gas and substrate temperatures are assumed to be constant, resulting in fixed probabilities for all thermal reactions.

Ion activated reactions usually have an energy dependence proportional to $\varepsilon^{1/2}$, where ε is the energy of the impinging

particle.[36] This dependence is implemented using the form

$$
P(\varepsilon) = p_0 \left(\frac{\varepsilon - \varepsilon_{th}}{\varepsilon_0 - \varepsilon_{th}} \right)^n, \tag{23}
$$

where $P(\varepsilon)$ is the energy dependent yield, having threshold energy ε_{th}, ε_0 is a reference energy, p_0 is the sputtering yield at the reference energy, and n is the energy dependent exponent (typically 1/2).

In addition to an energy dependence, most ion activated reactions also have a dependence on the angle of incidence of the impinging particle. This angular dependence can be significantly different for physical sputtering and chemically enhanced sputtering processes.[37] To distinguish these processes, two angular dependent probability functions, $P(\theta)$, are employed. One angular dependency typically has a maximum near a 60° angle of incidence, is less than unity at normal incidence and drops to zero at grazing incidence, characteristics of physical sputtering. The second angular dependency function is unity at normal incidence, gradually dropping after 45° until reaching zero at grazing incidence, characteristic of chemical sputtering. The total yield of a sputtering reaction is then given by

$$
P(\varepsilon, \theta) = P(\varepsilon)P(\theta). \tag{24}
$$

When a gas particle intersects with a surface, the probability of reaction is, by definition, unity. The process of choosing a particular reaction for a gas-solid pair requires a series of renormalizations. Since $P(\varepsilon, \theta)$ can exceed one, and there may be several energy dependent reactions between any gas/solid pair, the probability of the ith reaction must be renormalized so as to not exceed one,

$$
P_i(\varepsilon, \theta) = \frac{P_i(\varepsilon)P_i(\theta)}{\sum\limits_{j=1}^{N} P_j(\varepsilon)P_j(\theta)}, \tag{25}
$$

where N is the number of reactions between this gas/solid pair. If the sum of the unnormalized probabilities is less than one, then the probability of the elastic type (4) reaction is increased so the sum is unity. If the sum of the unnormalized probabilities is greater than one, then the probability of thermal reactions is scaled down so that the probability is unity. The normalized probabilities are converted to a cumulative probability distribution in the same manner as for choosing the initial velocity of a particle. Choice of a random number then determines which reaction occurs.

Atomic radical species, such as fluorine atoms, can diffuse through a steady-state polymer capping layer and play an important role in etching processes.[7,38] Since the MCFPM utilizes pseudoparticles, an atomistic approach was adopted in which a random walk through the computational lattice represents the diffusion of individual pseudoparticles through the polymer layer. Diffusion occurs with a user defined, fixed probability whenever a diffusible gas species strikes a surface of a permeable material, such as the

polymer. If such a particle interacts with a permeable surface but does not enter the material to diffuse, the particle diffusively reflects.

Diffusion of a particle through the permeable material takes place on the computational mesh, not in continuous space as with particles propagating in the gas phase or during implantation. When the particle begins to diffuse through the solid, the position of the particle projected onto the mesh as described by Eq. (9). The particle propagates through the mesh by randomly choosing its next location from the current set of six nearest neighbors (NNs). If the new chosen position is a gas phase cell, as would occur of the particle diffused back to the surface, the particle is reemitted from the solid at that point with a Lambertian angular distribution, similar to a thermal particle reflecting from the surface at that point. If the new position is a nonpermeable material, the interaction with that cell is treated in the same way as a gas phase particle interacting with a new surface site. For instance, if an F atom diffuses through a polymer overlayer and encounters an Si material site beneath the surface, there is a possibility that a reaction will occur forming SiF, consuming the F radical. If such a reaction does not occur with the nonpermeable material, a different nearest neighbor is chosen, and the particle continues propagating by random walk through the polymer layer.

To ensure that during the random walk the particle visits each nearest neighbor only once, the next position in the random walk is chosen from a shuffled list of possible transitions. First, a list of integers from 1 to 6 representing the nearest neighbors is generated. This list is then shuffled using the Fisher-Yates algorithm.[39] The first integer from the shuffled list is selected and mapped to the nearest neighbor transition from a static lookup table. If this neighbor does not result in an allowable transition (the new site is not polymer) or produces a reaction which consumes the diffusing particle, the next integer in the list is selected.

The species diffusing through, for example, polymer are often highly reactive. Some atomic species may only react with the underlying material, but most (F and O in particular) will also react with the polymer itself. Such thermal reactions are assigned a fixed probability, and this probability is evaluated at each step in the random walk. A cumulative probability array for reactions with the solid is constructed, and the choice of a random number determines whether the diffusing radical reacts with the polymer. As a result of these reactions, highly reactive species will have a smaller average depth of penetration (sampling a smaller volume surrounding the point of entering the solid) than less reactive particles, despite having the same mean free path.

Modeling of ion implantation phenomenon is necessary for capturing the physics of the fluorocarbon etching mechanism. Several physical processes, including energy transport to the etch front, mixing, and energy activated subsurface chemical reactions should be addressed. The MCFPM enables user defined energetic species to penetrate into solids and continue to propagate until a stochastically determined implant range is reached. The average implant range for each ion (hot neutral) for each solid material in the mechanism is

calculated using the stopping range of ions in matter (SRIM)[40] code. Then added into the MCFPM database.

The actual implant range for a specific ion and solid is randomly chosen from a Gaussian distribution with the mean range provided by the SRIM data with a standard deviation equal to half of the mean. For most ions of interest (e.g., Cl⁺, F⁺, O⁺, Ar⁺), this process produces a close match to the longitudinal straggle predicted by SRIM. During implantation, the particle is tracked through continuous 3D space, with a scattering event occurring each time the particle enters a new computational cell, resulting in an average mean free path of approximately $\Delta x = 0.3$ nm. At each scattering event, polar and azimuthal scattering angles are chosen using Monte Carlo techniques. The polar angle is selected from an exponential distribution with a user defined mean (7° was used for all results presented here). This mean polar scattering angle was adjusted to closely match the SRIM results for lateral straggle for typical ions (Ar⁺ and F⁺). The exponential distribution of polar angles results in mostly small-angle scattering, with the occasional high angle scattering event. The azimuthal angle is chosen from a uniform distribution of $[0, 2\pi)$. Scattering is implemented using the same Euler angle rotations described in Eqs. (17) and (18), substituting the current velocity vector for the surface normal vector.

There are several benefits to modeling the scattering of ions during implant as a series of discrete scattering events compared to a simpler line-of-sight technique. First, distributions of implanted ions more accurately reflect the true distribution, as shown by results from MCFPM in Fig. 1, produced by SRIM calculations. Second, including discrete subsurface scattering of ions enables the modeling of the reflection of quasi-grazing ion impacts. (That is, an ion that penetrates a surface, scatters beneath the surface, and exits the solid back into the gas phase.) All ions striking a solid surface with an incident angle greater than 1° are assumed to implant. For ions with small angles (quasi-grazing), scattering within the material results in a large fraction of implanting ions reemerging from the solid. Such particles continue to travel in the gas phase with the velocity and energy which they had when emerging from the implant path. The energy
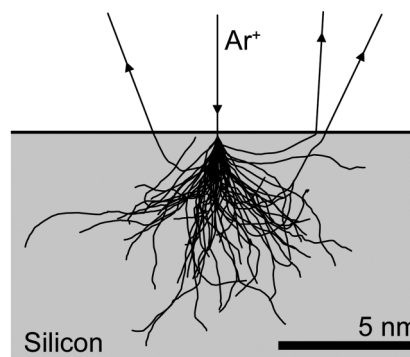

FIG. 1. Trajectories for 60 incoming 2000 eV Ar⁺ ions implanting into silicon predicted by the MCFPM. The implant range calculated from SRIM is 5 nm.

of the scattered particle is calculated as

$$\varepsilon = \varepsilon_i \left(1 - \exp\left[\alpha\left(\frac{l}{\Lambda} - 1\right)\right]\right), \tag{26}$$

where ε_i is the ion's initial energy, Λ is the implant range, l is the path length traveled, and α is a user defined parameter. A value of $\alpha = 8.0$ was used for all simulations presented here. The result is the reflection of quasi-grazing ions with a distribution of scattering angles and energies which are related to the implant properties of the particles. Similar distributions of scattering angle and energy have been observed experimentally and using molecular dynamics simulations.[41,42]

The collision cascade initiated by ion implantation deposits its energy into the solid, not only near the implant site, but also along the implant path due to electronic stopping forces and stochastic nuclear stopping.[40] To model this cascade, *ion induced mixing* was implemented whereby energy deposition is represented as the exchange of the material properties of two adjacent computational cells. This ion induced mixing occurs at each cell along the implant path with a probability defined by the user—100% is used for all simulations presented here. When a mixing event occurs, the material identity of the cell currently containing the ion is swapped with the material identity of a randomly chosen nearest neighbor. In the bulk of a homogeneous material, this mixing goes unnoticed, but near interfaces the results of ion mixing are critical.

When two solid materials are brought into contact due to ion induced mixing, there is a probability that a *solid-solid reaction* will occur. In the MCFPM, a solid-solid reaction represents the reaction of two chemical compounds in the solid phase that forms a new material. Since ion mixing represents energy deposition these reactions are effectively ion activated mixing processes at the scale of the computational cell. For example, our solid phase model of the SiO$_2$ etching reaction involves three materials: SiO$_2$, CF$_x$ polymer, and a selvedge layer SiO$_2$C$_x$F$_y$. This SiO$_2$C$_x$F$_y$ material represents the thin layer where C–O and Si–F bonds co-exist.[43] During etching, it is common for an ion implantation event to bring a CF$_x$ polymer cell in direct contact with an SiO$_2$ cell. In this case, a solid-solid reaction can occur which converts the CF$_x$ polymer cell and the SiO$_2$ cell into an SiO$_2$C$_x$F$_y$ cell due to the ion energy deposited in the lattice, such as

$$\text{SiO}_2 + \text{CF}_{x(s)} \rightarrow \text{SiO}_2\text{C}_x\text{F}_y. \tag{27}$$
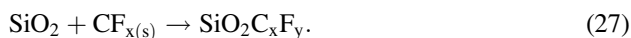
Since the reaction between SiO$_2$ and CF$_{x(s)}$ in Eq. (27) results in two solid material cells reacting to form one new solid cell, a vacancy is generated at the interface between the polymer and SiO$_2$. This vacant cell must be addressed in the model, or the polymer surface would become porous, eventually become artificially separated from the SiO$_2$ surface. (The polymer is assumed to remain dense during this reaction.) To prevent this artificial porosity, the resulting vacancy is diffused out of the polymer, using an algorithm identical to the process of neutral diffusion previously described

where the reaction probability is zero. The vacancy diffusion proceeds by a random walk through the polymer overlayer until the particle reaches a gas cell, at which point the vacancy is released to the gas phase. This diffusion of the vacancy was necessary due to the inability to a priori specify the direction in which a polymer overlayer would be "compressed" to eliminate an *in situ* vacancy.

In order to speed the rejection of vacancies, materials that are nonpermeable to vacancies can be specified. For example, if there is an underlying etch stop layer which is known to always be at the bottom of the feature, this material can be denoted as nonpermeable. The vacancy will then reflected from that nonpermeable material in a direction more likely to find the solid-gas boundary.

In addition to solid-solid reactions which occur due to the energy transfer from the implanting ion to the solid, it is also possible for the ion to undergo reactions at subsurface interfaces. Selection of these reactions is performed in the same manner as for reactions at the gas/solid interface—construction of a cumulative probability array and choice of a random number. The ion energy that produces the reaction at the subsurface site will have been appropriately scaled by Eq. (26) due to energy losses during implantation. Such reactions can, for example, result in sputtering which generates a vacancy in the solid. Such vacancies diffuse to the gas surface in the same manner as for vacancies generated by solid-solid reactions. Subsurface reactions can also produce a gas phase volatile product such as SiF$_4$ or CO. If the product is nonreactive, it is not tracked in the simulation, assuming that it will eventually diffuse out of solid (and feature as a whole) without having reacted. If the gas phase product is a radical (e.g., F, CF$_2$, SiF), then the particle is diffused out of the solid and into the gas phase using the neutral diffusion technique as previously described. This procedure results in some probability of the product reacting with the polymer layer before emerging into the gas phase.

When an ion reaches the end of its implant path, there are several possible outcomes. It is possible that the implanting ion will generate interstitial defects. Depending on the size of the ion, this type of defect can be modeled in different ways in the MCFPM. For large nonreactive atoms (e.g., heavy ions—Ar, Xe), a new cell can be generated in the lattice, displacing a (randomly chosen) nearest neighbor cell. This displaced cell will then displace one of its neighboring cells, continuing in a random walk until one of the displaced cells reaches a surface by displacing a gas cell. The algorithm is similar to the diffusion of radical species discussed previously, with the exception that the material identity of each cell in the random walk path will be replaced with the material of the previous cell. The end result is that each atom along the random walk path is pushed one cell in the direction of the displaced particle. This random walk behavior is intended to model the secondary collision cascade(s) which occur due to atoms displaced by primary "knock-on" ion impacts.[44] For smaller nonreactive ions (e.g., He, Ne), the interstitial defect may be neglected, resulting in no change to the lattice at the end of the implant range. For more reactive ions, such as F$^+$, Cl$^+$, or O$^+$, substitutional defects may form,

effectively acting as subsurface chemical reactions. For instance, Cl^+ implanting into silicon can generate an SiCl cell at the implant site.

The MCFPM can also address the diffusion of adsorbed particles on surfaces. This type of diffusion is particularly important in depositing chemistries, such as PECVD or polymerizing fluorocarbon plasmas to prevent dendritic growth. In the simulations presented here, the polymer species, $CF_{x(s)}$, deposited by the sticking of $CF_{x(g)}$ is allowed to diffuse along the surface to ensure conformal polymer film formation. In this process, species are designated as being physisorbed species or chemisorbed. When, for example, a $CF_{x(g)}$ radical deposits onto the surface as a physisorbed species, the particle is propagated along the surface using a Metropolis-like algorithm to minimize the Hamiltonian function,

$$\hat{H} = U^{\mathrm{M}} + U^{\mathrm{H}} + U^{\mathrm{G}}. \tag{28}$$

The three terms in this Hamiltonian represent the contributions of neighboring solid cells through the Morse binding potential (U^{M}), the energy penalty for hopping to next-nearest-neighbor sites (U^{H}), and a phenomenological potential which attracts the deposited material toward a "base" material (U^{G}).

The Morse potential is the dominant term in most systems. This term represents the potential between two solid cells as

$$U_{ij}^{\mathrm{M}} = V_M \left[exp\left(-\frac{2(r_{ij} - r_0)}{A_0} \right) - 2exp\left(-\frac{r_{ij} - r_0}{A_0} \right) \right], \tag{29}$$

where $r_{ij} = \|\mathbf{r}_i - \mathbf{r}_j\|$ is the distance between cells i and j. The variables V_{M}, r_0, and A_0 have user defined values that scale the potential (U^M), define the distance of strongest binding (r_0), and define the width of the binding well (A_0). A value of $V_M = 5$ meV was used for this study. The general assumption of using this potential is that having more close neighbors produces more binding energy than fewer neighbors. To achieve this end $r_0 = \Delta x = 3$ Å so that NNs contribute the largest (most negative) binding energies. (In this cubic lattice, nearest neighbors are cells that share a face with the cell in question, next-nearest neighbors share an edge and next-next-nearest neighbors share a corner point) The width of the binding region, A_0, can be adjusted to provide larger or smaller contributions from next-nearest-neighbors (NNNs) and next-next-nearest-neighbors (4N). The value of A_0 used for this study was 1 Å. Contributions from cells beyond 4N are not considered regardless of the value of A_0.

The hopping potential represents an energy penalty for the physisorbed species hopping to an NNN site instead of an NN site. It is evaluated as

$$U_{ij}^{\mathrm{H}} = \begin{cases} 0 & \mathrm{NN} \\ V_H & \mathrm{NNN} \\ \infty & \mathrm{otherwise} \end{cases}, \tag{30}$$

where V_{H} is the user defined energy penalty in eV ($V_H = 5$ meV was used in this study). Hopping to 4N or further in a single step is not allowed. Allowing for NNN hopping is required to diffuse across steps in the cubic lattice. Otherwise, diffusion would be limited to only smooth surfaces.

The phenomenological attractive potential, U^{G}, is used to enable smooth and conformal coatings when diffusion with only Morse and hopping potentials does not suffice. This potential term offers an empirical method to force the polymer deposition to favor smooth and conformal films matching experimental results. The attractive potential is calculated as

$$U_{ij}^{\mathrm{G}} = V_G(D_j - D_i), \tag{31}$$

where V_G is the strength of the attractive potential in eV/Δx and D_i is the distance from cell i to the nearest *base material* in units of Δx. A value of $V_G = 50$ meV was used for all simulations presented here. This method enables a set of base materials to direct the depositing species. To quickly calculate D_i, the MCFPM periodically calculates the distance from each gas cell in the mesh to the nearest base material. This distance is stored as a scalar field, which can be quickly evaluated during the diffusion process. As long as this distance field is updated frequently enough, this technique offers a way to empirically tune the smoothness of the deposited film.

The distance field is calculated using a rapid but approximate method. The simplest method which provides an exact result would involve looping through the entire mesh for each point on the mesh to look for the nearest base material. The work for this method would scale as O(n^2) where n is the number of cells in the mesh. Instead, an iterative method is employed, looping through the mesh several times to build the solution. On the first pass through the mesh, cells which have a base material nearest neighbor are assigned a distance value of 1, cells which are next-nearest-neighbors with a base material are assigned a value of $\sqrt{2}$, and 4N cells are assigned $2\sqrt{2}$. On subsequent passes, cells that have neighbors with distance values are assigned the value of the neighbor cell with the smallest distance value plus 1 for nearest neighbors, $\sqrt{2}$ for NNN, and $2\sqrt{2}$ for 4N. In this way, the distance field can be calculated by looping through the mesh a number of times, m, that can be significantly less than the number of cells in the mesh, resulting in O(n) algorithm scaling. If m is equal to the number of cells in the largest side of the computational domain, the entire distance mesh will be calculated. If m is smaller, cells which are not given a distance value by the algorithm are assumed to be infinitely far from the base material. This allows for values of m which address typical film thicknesses without needing to calculate the entire mesh. In the work presented here, the algorithm uses $m = 40$ iterative loops, while n is typically 10^6–10^7.

The diffusion of physisorbed particles proceeds as discrete hopping events which are chosen using a similar technique to the Metropolis-Hastings algorithm.[45] If the particle

is currently at position i, a new proposed position, j, is chosen randomly from a list of all NN and NNN sites. The potential difference between these sites, ΔE_{ij} in eV, is calculated as

$$\Delta E_{ij} = \left(\sum_n^{N_i} U_{in}^M - \sum_n^{N_j} U_{jn}^M \right) + U_{ij}^H + U_{ij}^G, \qquad (32)$$

where N_i is the set of all NN, NNN, and 4N of site i. The proposed transition is accepted with probability

$$P_{i \to j} = \begin{cases} 1 & \text{if} \quad \Delta E_{ij} < 0 \\ \exp\left(-\dfrac{\Delta E_{ij}}{k_B T} \right) & \text{if} \quad \Delta E_{ij} \geq 0 \end{cases}, \qquad (33)$$

where k_B is Boltzmann's constant and T is the substrate temperature ($T = 313$ K in this study). Regardless if the transition is accepted or rejected, the particle will undergo another diffusion step with probability P_d, which is a user defined parameter ($P_d = 0.99$ here) to regulate the amount of diffusion to be allowed. Note that even if high values of P_d are chosen, the particle will likely remain trapped if the particle finds a potential well where $\Delta E_{ij} \gg k_B T$ for all possible transitions. This process continues, choosing a new random number each step, until a number is chosen which is greater than P_d. This process allows a reasonable large jumps to, for example, escape from a potential well. When diffusion is complete, the physisorbed species is converted to the corresponding chemisorbed species.

The value of V_M (5 meV) was chosen so there would be significant diffusion at the assumed substrate temperature of 313 K. The value of A_0 (1 Å) was based by analogy to previous studies of surface diffusion using Morse potentials.[46] V_H (5 meV) was chosen to limit unrealistically long hops. V_G (50 meV) was empirically chosen to produce nonporous films.

Many computational metrics, including etch rate and height, are averaged over part or all of the computational domains. For instance, the height of the feature is calculated by finding the highest solid cell for each xy position in the mesh. In blanket etching, the reported height is then the average of these heights over the entire computational domain. In feature simulations where a portion of the profile is masked, the average can be taken over a smaller window of xy positions so that the measurement only represents the height of the etch front itself. The height is measured with a user defined frequency, and the etch rate is calculated as the first order finite difference with respect to time. The period at which the height is periodically measured varies depending on the rate of change of the process being measured, from 0.05 s for the passivation phase of ALE to >1 s for continuous etching.

III. SURFACE REACTION MECHANISM FOR SiO₂, Si₃N₄, AND Si ETCHING IN FLUOROCARBON PLASMAS

A new reaction mechanism was developed for the interaction between reactive species produced in an Ar/C₄F₈ plasma and SiO₂, Si₃N₄, and Si. This mechanism heavily relies on the transport of reactive and energetic species through the polymer overlayer. This mechanism should be applicable to the majority of fluorocarbon plasmas that produce similar varieties of radicals.

The lowest energy etching reaction pathway involves five steps:

1. Passivation of the surface by $CF_{x(g)}$ radicals, forming a selvedge layer where C–O, C–N, and/or Si–F bonds exist.
2. Deposition of a finite thickness polymer layer on top of the selvedge layer.
3. O or N removal from the solid by chemical sputtering leaving $SiF_{x(s)}$, activated by ions penetrating through the polymer layer.
4. Etching of $SiF_{x(s)}$ by chemical sputtering (by implanting ions) or thermal reactions with fluorine radicals diffusing through the polymer.
5. Repassivation of the underlying surface by ion mixing of surface sites with the polymer overlayer. (Repeat steps 2–5.)

In addition to the reactions which make up the minimum energy etching pathway, many other reactions are possible and necessary for a complete description of the fluorocarbon etching mechanism. In this section, a description is given of the reactions involved, with a complete list of possible reactions included in this mechanism given in Table I.

The mechanism relies on the formation of two distinct material regions in the overlayer which forms on the substrate, the selvedge layer, and the polymer layer. The selvedge layer is the thin region where covalent bonds exist between the fluoropolymer overlayer and the underlying material. For SiO₂, this region is modeled using the species $SiO_2C_xF_{y(s)}$, $SiOC_xF_{y(s)}$, and $SiF_{x(s)}$, consistent with the experiments of Gasvoda *et al.*[47] For Si₃N₄, the selvedge layer is composed of $SiNC_xF_y$ and $SiF_{x(s)}$ species. On top of the selvedge layer, a fluoropolymer [denoted $CF_{x(s)}$] layer forms which is unaffected by the substrate material being etched. Taken together, the selvedge and polymer layers will be referred to as the *overlayer*.

The selvedge species in the SiO₂ system, $SiO_2C_xF_{y(s)}$, $SiOC_xF_{y(s)}$, and $SiF_{x(s)}$, represent different phases in the etching process. The $SiO_2C_xF_{y(s)}$ species represents a site where a $CF_{x(g)}$ molecule has chemisorbed to an SiO₂ site, by the formation of either a C–O or an Si–F bond. The $SiOC_xF_{y(s)}$ material is a site which has undergone deoxygenation due to an ion impact reaction, such as

$$SiO_2C_xF_{y(s)} + Ar_{(g)}^+ \to SiOC_xF_{y(s)} + CO_{(g)} + Ar_{(g)}. \qquad (34)$$

This reaction converts the initial $SiO_2C_xF_{y(s)}$ cell to

TABLE I. Fluorocarbon surface reaction mechanism.

	Reaction	p^a	ε_{th}^a (eV)	p_0^a	ε_0^a (eV)	Ang[b]	Notes
	Polymer deposition reactions						
1	$Si_{(s)} + CF_{(2)(g)} \rightarrow Si_{(s)} + CF_{x(s)}$	0.20					c
2	$SiO_{2(s)} + CF_{(2)(g)} \rightarrow SiO_2C_xF_{y(s)}$	0.20					c
3	$Si_3N_{4(s)} + CF_{(2)(g)} \rightarrow SiNC_xF_{y(s)}$	0.20					c
4	$SiO_2C_xF_{y(s)} + CF_{(2)(g)} \rightarrow SiO_2C_xF_{y(s)} + CF_{x(s)}$	0.20					c
5	$SiOC_xF_{y(s)} + CF_{(2)(g)} \rightarrow SiOC_xF_{y(s)} + CF_{x(s)}$	0.20					c
6	$SiNC_xF_{y(s)} + CF_{(2)(g)} \rightarrow SiNC_xF_{y(s)} + CF_{x(s)}$	0.20					c
7	$CF_{x(s)} + CF_{(2)(g)} \rightarrow CF_{x(s)} + CF_{x(s)}$	0.01					c
8	$CF_x^*{}_{(s)} + CF_{(2)(g)} \rightarrow CF_{x(s)} + CF_{x(s)}$	0.03					c, d
9	$CF_{x(s)} + CF^*_{(implant)} \rightarrow CF_{x(s)} + CF_{x(s)}$	1.00					e
	Polymer loss reactions						
10	$CF_{x(s)} + F_{(g)} \rightarrow CF_{4(g)}$	0.008					
11	$CF_x^*{}_{(s)} + F_{(g)} \rightarrow CF_{4(g)}$	0.004					d
12	$CF_{x(s)} + Ar_{(g)}^+ \rightarrow CF_{x(g)} + Ar$		30	0.030	100	P	
13	$CF_{x(s)} + C_xF_{y(g)}^+ \rightarrow CF_{x(g)} + CF_{(2)(g)}$		30	0.003	500	P	c
14	$SiO_{2(s)} + CF_{x(s)} + M^+ \rightarrow SiO_2C_xF_{y(s)}$	1.00					f
15	$Si_3N_{4(s)} + CF_{x(s)} + M^+ \rightarrow SiNC_xF_{y(s)} + CF_{x(s)}$	1.00					f
	Polymer activation						
16	$CF_{x(s)} + Ar_{(g)}^+ \rightarrow CF_x^*{}_{(s)} + Ar_{(g)}$		150[g]	0.03[g]		C	d
17	$CF_{x(s)} + C_xF_{y(g)}^+ \rightarrow CF_x^*{}_{(s)} + F_{(implant)}^+ + C_xF_{y(g)}$		60[g]	0.30[g]		C	d
18	$CF_{x(s)} + C_xF_{y(g)}^+ \rightarrow CF_x^*{}_{(s)} + CF^*_{(implant)} + F_{(implant)}^+$		30[g]	0.10[g]		C	d
19	$CF_{x(s)} + C_xF_{y(g)}^+ \rightarrow CF_{x(s)} + F_{(implant)}^+ + C_xF_{y(g)}$	0.95					
20	$CF_{x(s)} + C_xF_{y(g)}^+ \rightarrow CF_{x(s)} + F_{(implant)}^+ + CF_{(2)(g)}$	0.05					c
	Silicon reactions						
21	$Si_{(s)} + F_{(g)} \rightarrow SiF_{(s)}$	0.90					
22	$SiF_{(s)} + F_{(g)} \rightarrow SiF_{2(s)}$	0.50					
23	$SiF_{2(s)} + F_{(g)} \rightarrow SiF_{3(s)}$	0.50					
24	$SiF_{3(s)} + F_{(g)} \rightarrow SiF_{2(s)} + F_{2(g)}$	0.01					
25	$SiF_{3(s)} + F_{(g)} \rightarrow SiF_{4(g)}$	0.10					
26	$X_{SiF(s)} + F_{(g)} \rightarrow SiF_{4(g)}$	0.90					
27	$Si_{(s)} + M_{(g)}^+ \rightarrow Si_{(g)} + M_{(g)}$		50	0.010	200	P	
28	$SiF_{x(s)} + M_{(g)}^+ \rightarrow SiF_{x(g)} + M_{(g)}$		10	0.010	200	C	
29	$SiF_{x(s)} + M_{(g)}^+ \rightarrow SiF_{x(g)} + M_{(g)}$		150	0.010	200	P	
	Oxide reactions						
30	$SiO_{2(s)} + M_{(g)}^+ \rightarrow SiO_{2(g)} + M_{(g)}$		70	0.010	140	P	
31	$SiO_{2(s)} + C_xF_{y(g)}^+ \rightarrow SiO_{2\ (s)} + CF_{(2)(g)}$	0.05					c
32	$SiO_{2(s)} + C_xF_{y(g)}^+ \rightarrow SiO_2C_xF_{y(s)}$	0.80					
33	$SiO_2C_xF_{y(s)} + F_{(g)} \rightarrow SiO_2C_xF_{y(s)} + F_{2(g)}$	0.01					
34	$SiO_2C_xF_{y(s)} + C_xF_{y(g)}^+ \rightarrow SiO_2C_xF_{y(s)} + CF_{(2)(g)}$	0.05					c
35	$SiO_2C_xF_{y(s)} + C_xF_{y(g)}^+ \rightarrow SiO_2C_xF_{y(s)} + CF_{x(s)}$	0.80					
36	$SiO_2C_xF_{y(s)} + M_{(g)}^+ \rightarrow SiOC_xF_{y(s)} + CO(F_2)_{(g)} + M_{(g)}$		10	0.800	75	C	
37	$SiO_2C_xF_{y(s)} + M_{(g)}^+ \rightarrow SiF_{4(g)} + CO(F_2)_{(g)} + M_{(g)}$		50	0.800	100	C	
38	$SiO_2C_xF_{y(s)} + M_{(g)}^+ \rightarrow SiF_{4(g)} + CO(F_2)_{(g)} + M_{(g)}$		100	0.800	125	P	
39	$SiOC_xF_{y(s)} + C_xF_{y(g)}^+ \rightarrow SiOC_xF_{y(s)} + CF_{(2)(g)}$	0.05					c
40	$SiOC_xF_{y(s)} + C_xF_{y(g)}^+ \rightarrow SiOC_xF_{y(s)} + CF_{x(s)}$	0.80					
41	$SiOC_xF_{y(s)} + M_{(g)}^+ \rightarrow X_{SiF(s)} + CO(F_2)_{(g)} + M_{(g)}$		10	0.800	75	C	
42	$SiOC_xF_{y(s)} + M_{(g)}^+ \rightarrow SiF_{4(g)} + CO(F_2)_{(g)} + M_{(g)}$		50	0.800	100	C	
43	$SiOC_xF_{y(s)} + M_{(g)}^+ \rightarrow SiF_{4(g)} + CO(F_2)_{(g)} + M_{(g)}$		100	0.800	125	P	
	Nitride reactions						
44	$Si_3N_{4(s)} + M_{(g)}^+ \rightarrow Si_3N_{4(g)} + M_{(g)}$		70	0.010	140	P	
45	$Si_3N_{4(s)} + C_xF_{y(g)}^+ \rightarrow Si_3N_{4(s)} + CF_{(2)(g)}$	0.05					c
46	$Si_3N_{4(s)} + C_xF_{y(g)}^+ \rightarrow SiNC_xF_{y(s)}$	0.80					
47	$SiNC_xF_{y(s)} + F_{(g)} \rightarrow SiNC_xF_{y(s)} + F_{2(g)}$	0.01					
48	$SiNC_xF_{y(s)} + C_xF_{y(g)}^+ \rightarrow SiNC_xF_{y(s)} + CF_{(2)(g)}$	0.05					c
49	$SiNC_xF_{y(s)} + C_xF_{y(g)}^+ \rightarrow SiNC_xF_{y(s)} + CF_{x(s)}$	0.80					
50	$SiNC_xF_{y(s)} + M_{(g)}^+ \rightarrow X_{SiF(s)} + CNF_{(g)}$		30	0.20	75	C	
51	$SiNC_xF_{y(s)} + M_{(g)}^+ \rightarrow SiF_{4(g)} + CNF_{(g)}$		50	0.20	100	C	
52	$SiNC_xF_{y(s)} + M_{(g)}^+ \rightarrow SiF_{4(g)} + CNF_{(g)}$		100	0.20	125	P	

[a]If ε_{th} and p_0 are blank, the reaction has no energy dependency, and the reaction probability, p, is constant.

[b]Angular dependence of the reaction. P = physical sputtering, C = chemical sputtering, blank for reactions with no angular dependency.

[c]$CF_{(2)(g)}$ represents the sum of CF and CF$_2$ flux.

[d]$CF_x^*{}_{(s)}$ represents the ion activated polymer, discussed in Sec. III.

[e]Reaction at the end of implant path. Described in Sec. III.

[f]Solid-solid reaction. Occurs due to ion activation energy supplied by M$^+$.

[g]Activation reaction. Probability drops linearly from p_0 at 5 eV to zero at ε_{th}.

SiOC$_x$F$_{y(s)}$, releasing a CO$_{(g)}$ etch product. Due to the strong C–O bond, this reaction is considered a chemically enhanced sputtering reaction in this mechanism, with a low energy threshold (ε_{th}) of 10 eV. The SiOC$_x$F$_{y(s)}$ can then be deoxygenated again by ion impact, resulting in an SiF$_{x(s)}$ site. Finally, the SiF$_{x(s)}$ site can be sputtered by low energy ions due to the strength of the Si–F bond weakening the strength of the bonding with the underlying lattice, or it can be thermally etched by fluorine radicals. This process is schematically shown in Fig. 2. These materials are not intended to representative individual molecules, but rather the average behavior of the materials in the computational cell. Due to this averaged behavior, the exact stoichiometry of each reaction is not necessarily conserved. The etching of Si$_3$N$_4$ proceeds through a similar pathway, but with only two selvedge materials, SiNC$_x$F$_{y(s)}$ and SiF$_{x(s)}$. For each silicon atom removed from the substrate, only one carbon atom is removed, as opposed to two carbon atoms in the case of the SiO$_2$C$_x$F$_{y(s)}$ etching channel. As a result, less polymer is consumed during the etching of Si$_3$N$_4$ compared to SiO$_2$.

Each of the selvedge species has a reduced surface binding energy compared to the underlying lattice, meaning that it is also possible to directly chemically sputter SiO$_2$C$_x$F$_{y(s)}$ or SiOC$_x$F$_{y(s)}$, instead of following the pathway described above. Direct chemical sputtering of each of these
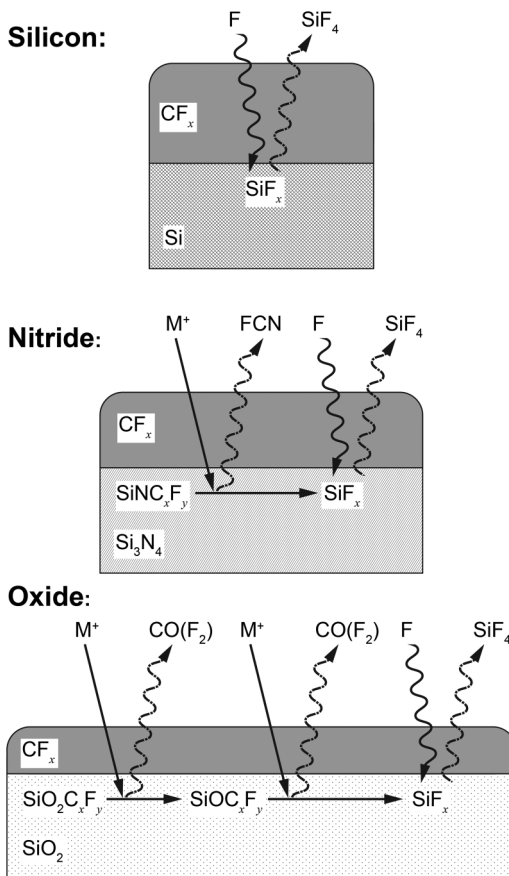
materials is included in the model, but with higher energy thresholds (14–30 eV) and lower probability than the lowest energy pathway described above. As a result, with predominantly low energy ions (as used for ALE) the multistep process dominates. With higher ion energy (>100 eV), direct sputtering of SiO$_2$C$_x$F$_{y(s)}$, SiOC$_x$F$_{y(s)}$, and SiNC$_x$F$_{y(s)}$ becomes the dominant etching pathway. Higher energy ions can also initiate physical sputtering reactions which directly remove SiO$_2$ or Si$_3$N$_4$. Physical sputtering reactions for these materials are given a higher threshold energy (70 eV) and lower probability than chemical sputtering reactions.

The formation of a steady-state polymer overlayer is critical to the fluorocarbon plasma etching mechanism, as described in Sec. I. In this mechanism, the steady-state behavior is achieved by allowing for chemisorption of CF and CF$_2$ radicals on the surface of the polymer, sputtering of polymer, and etching of the polymer by fluorine radicals which diffuse through the polymer volume. This process results in a deposition term in Eq. (1) which is proportional to the surface area, and a loss term that has components proportional to the polymer volume. The mechanism used for this study includes deposition from CF and CF$_2$ radicals due to their higher number of radical sites making them more reactive in general, though including deposition by CF$_3$ (or C$_n$F$_x$, n > 1) can be easily incorporated into the mechanism.

CF$_2$ in particular has a high abundance in the gas phase chemistries used here and has been experimentally shown to play an important role in polymerization.[48] The sum of the polymerizing species, CF and CF$_2$, will be referred to as CF$_{(2)}$ for brevity. The main polymer loss term is etching by fluorine radicals, as has been experimentally proposed.[5,7,38] Polymer etching by fluorine is a thermally driven process given a fixed probability of 0.008 in our model. This probability is the likelihood of the F atom etching the polymer at any step during the diffusion of the F radical through the polymer. The average likelihood of an etching event occurring per F$_{(g)}$−CF$_{x(s)}$ interaction is much higher than this value due to the multiple interactions. The exact value of this rate was adjusted to result in steady-state polymer thicknesses similar to experimental results during continuous etching.[5] In addition to polymer etching by fluorine radicals, ion sputtering of the polymer surface is also included in the model with a threshold energy of 30 eV. Despite the relatively low threshold, the sputtering reaction is given a low probability to conform with experimental observation that sputtering plays a minor role in polymer loss in this system.[7]

This model also includes a polymer activation channel, whereby low energy ions can create activated polymer sites which have a larger sticking coefficient for CF$_{(2)}$ radicals. This polymer activation mechanism models the breaking of bonds within the polymer layer, exposing a larger dangling bond density on the surface. This mechanism has been proposed to explain the higher polymer deposition rate in etch features with direct exposure to low energy ions, compared to neutral deposition of CF$_{(2)}$ radicals without such exposure.[49,50] The ion activation process is given a negative energy dependence to model the balance between ion activation at low energies and sputtering of polymer at higher ion

FIG. 2. Schematic of the Si, Si$_3$N$_4$, and SiO$_2$ etching mechanisms. The term M$^+$ denotes activation from any ion or hot neutral. Straight lines through the polymer overlayer imply ion implantation, while wavy lines represent diffusion through the overlayer.

energies. This results in the polymer deposition term, and therefore steady-state polymer overlayer thickness, that depends on the ion energy reaching the surface.[5] The sticking coefficients for CF$_{(2)}$ on SiO$_2$, unactivated polymer, and activated polymer are 0.20, 0.01, and 0.03, respectively. These sticking coefficients are similar to those obtained recently by Kaler *et al.* in cyclic plasma beam exposure experiments.[51]

The transfer of ion energy through the polymer overlayer to the etch front is critical to this etch mechanism. Which energetic particles carry the activation energy to the etch front is difficult to analyze. In this mechanism, Ar$^+$ is allowed to penetrate the polymer overlayer and react below the surface, a flux that is important during the ion bombardment phase of ALE where Ar$^+$ is the dominant flux. During continuous etching in C$_4$F$_8$/Ar plasmas, though, the dominant ions are C$_3$F$_5^+$ and C$_2$F$_4^+$. Even at the relatively low ion energies used in this study, the total kinetic energy of the arriving ion exceeds the bond energy of the molecule, implying that fragmentation of these larger ions is to be expected. Fragmentation of such ions for energies of tens to hundreds of eV has been investigated using first principles.[52] To account for fragmentation, large ions are allowed to dissociate into two fragments in the model, F$^+$ and CF*. The F$^+$ particle carries the majority of the ion energy through the film to deliver energy to the etch front. Fluorine was chosen to be the ion energy carrier because once it has cooled it will act as a source of fluorine radicals, as has been previously proposed as a result of large fluorocarbon fragmentation.[7,38] The CF* particle is a model construct which allows the CF$_{x(g)}$-like remains of the larger molecule to imbed in the polymer matrix forming a new polymer site. This process couples the polymer deposition rate to the C$_x$F$_y^+$ flux, as has been seen experimentally.[53]

IV. Ar/C$_4$F$_8$ INDUCTIVELY COUPLED PLASMAS

Properties of inductively coupled plasmas sustained in Ar/C$_4$F$_8$ mixtures for a reactor measuring 54 cm in diameter were computationally investigated using the HPEM. In this reactor design, a 300 mm wafer is mounted on a substrate biased with a RF power supply at 10 MHz. A four turn coil antenna is located 16.5 cm above the wafer, behind a quartz window. RF current (at 10 MHz) is passed through this antenna, which delivers power to the plasma by inductive coupling. The reactor is maintained at 20 mTorr, regulated by a feedback controlled gate valve, with a flow of 600 sccm of feedstock gas.

To simulate the two-step ALE process, passivation, and ion bombardment, simulations were performed with two different feedstock gases; an Ar/C$_4$F$_8$ = 95/5 mixture and Ar with trace (100 ppm) C$_4$F$_8$ contamination. For the remainder of this paper, the Ar/C$_4$F$_8$ = 95/5 mixture will be referred to as *FC gas*, and the argon gas with 100 ppm C$_4$F$_8$ will be referred to as *impure argon*. The C$_4$F$_8$ contamination in the impure argon gas is intended to represent the fluorocarbon impurities which can originate from incomplete purging of gas lines or desorption of fluorocarbon species from the

walls during the ion bombardment phase of ALE pulsing. The FC gas mixture will be used to model both continuous etching and passivation during ALE pulsing.

The FC gas mixture was investigated using inductive powers of 300 W and 1200 W. Since the pressure and feedstock flow rate were kept constant, the higher power produced significantly more dissociation of the C$_4$F$_8$ and larger fluxes of CF$_x$ radicals to the substrate. The total dissociation fraction (measured as the reactor averaged number of carbon atoms in dissociated fragments divided by the total number of carbon atoms in the reactor) for 1200 W was 0.44, compared to 0.18 for the 300 W plasma. The flux of neutral species to the wafer, shown in Fig. 3(a), indicates fluxes of F and CF$_x$ radicals generally increase at 1200 W relative to 300 W due to the larger rate of dissociation of C$_4$F$_8$, while the flux of C$_2$F$_4$ decreases, a primary dissociation product of C$_4$F$_8$. This trend indicates that the higher power is also dissociating the primary dissociation products of C$_4$F$_8$, which then contributes to the fluxes of CF$_x$ and F. The ratio of fluorine radicals to polymerizing fluorocarbon radicals [F/CF$_{(2)}$]
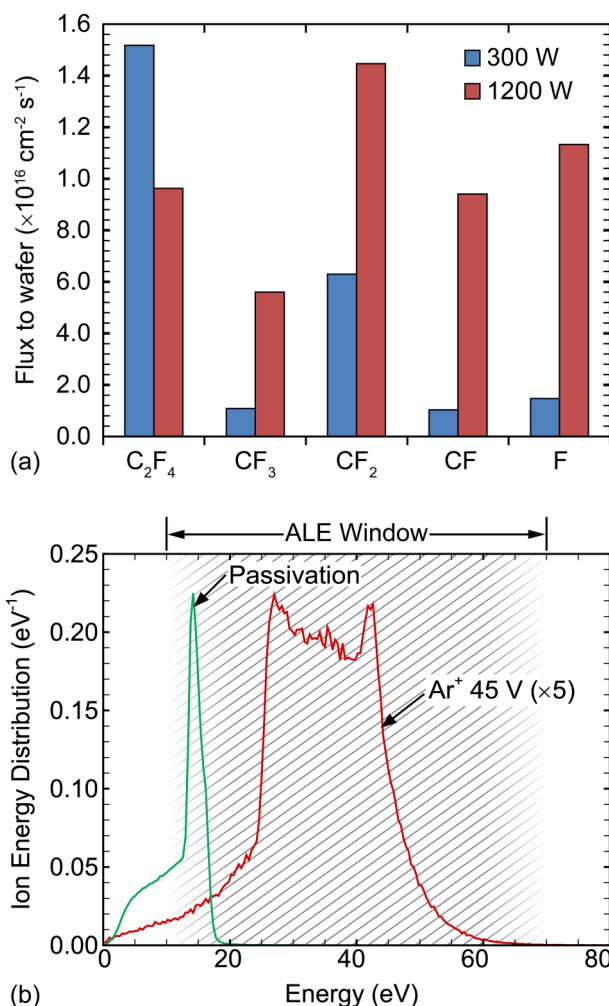

(a)

(b)

FIG. 3. Plasma conditions used in continuous and ALE processing. (a) Ratios of fluxes of C$_4$F$_8$ dissociation products incident onto the wafer for ICP powers of 300 and 1200 W. (b) Ion energy distributions reaching the surface during the passivation (V_{RF} = 0 V) and ion bombardment (V_{RF} = 45 V) phases.

is therefore higher in the 1200 W plasma (0.47) than in the 300 W plasma (0.2).

The energy of ions impinging on the wafer can be adjusted by applying an RF bias voltage, V_{RF}, to the substrate without significantly perturbing other plasma parameters. By varying V_{RF} (amplitude) from 20 to 100 V, values relevant to ALE processes, the DC bias changes from −6 to −70 V, producing average ion energies onto the wafer of 21–85 eV. The natural floating sheath potential results in an average ion energy of 14 eV with $V_{RF} = 0$. Due to the large range of ion masses [a low of 19 atomic mass unit (AMU) for F^+ to 131 AMU for $C_3F_5^{\pm}$], the IED becomes bi-modal as V_{RF} increases. The shape of the IED is important in ALE applications. Even though the average ion energy may be within the ALE window (energies greater than the threshold for sputtering passivated sites but less than sputtering bare sites), the maximum energy of the IED may exceed the sputtering threshold of bare sites. Having ion energies above the ALE window has important implications to ALE processing by enabling continuous etching processes. The power deposition by the RF bias voltage (44 W for $V_{RF} = 100$ V) is dominantly dissipated in ion acceleration and a small amount of additional dissociation. The total ion flux varies by only about 10%, 3.0×10^{15} to 3.4×10^{15} cm^{-2} s^{-1}, for a range of V_{RF} from 0 to 100 V, with the primary ions being $C_3F_5^+$ and $C_2F_4^+$. The fluxes of reactive neutral species to the wafer also do not significantly change when applying the bias, varying by <7% with V_{RF} from 0 to 100 V.

While continuous etching and ALE surface passivation can be conducted using the FC mixture, ALE ion bombardment is usually performed in pure inert gas, often argon. Unfortunately, it is difficult to completely eliminate fluorocarbon gas from the reactor after the passivation phase due to incomplete purging of gas from fore-lines and desorption of species from the reactor walls under ion bombardment.[48,54–56] Such fluorocarbon contamination in the ion bombardment phase may have significant effects on ALE performance. To model this contamination, simulations of the ion bombardment phase of ALE were conducted in the impure argon gas mixture. The impure argon plasma was sustained with 600 W of ICP power. The pressure and feed-gas flow rate were 20 mTorr and 600 sccm. These conditions result in an Ar^+ flux to the wafer of 6.9×10^{15} cm^{-2}s^{-1}. The flux of polymerizing radicals is 2.2×10^{15} cm^{-2} s^{-1} and that of fluorine radicals is 1.3×10^{15} cm^{-2} s^{-1}. RF biases from 40 to 100 V were investigated. A bias of $V_{RF} = 45$ V results in an average ion energy of 34 eV delivered to the substrate in a bi-modal energy distribution having a high energy peak at 42 eV. This IED fits well into the ALE window, as shown in Fig. 3(b), and will be used for all cases unless otherwise noted. (Recall that the ALE window is the energy range between the thresholds of ion activated chemical sputtering of the polymer-dielectric complex and that of physical sputtering.)

Continuous etching of SiO$_2$, Si$_3$N$_4$, and Si can be achieved using the FC gas mixture and modest bias voltages, as shown in Fig. 4. Continuous etching is not the focus of this investigation, but it is important to evaluate the new polymer etching mechanism against known trends in continuous
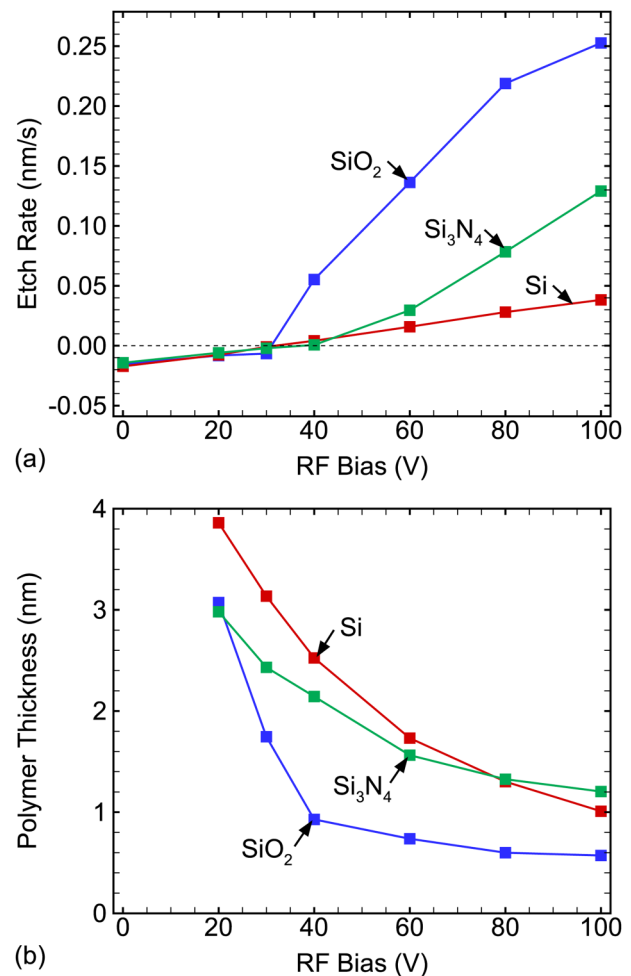

(a)

(b)

FIG. 4. Continuous etching properties of Si, SiO$_2$, and Si$_3$N$_4$ using the FC gas mixture as a function of RF bias voltage. (a) Etch rate, where positive values represent continuous etching and negative values are the average polymer deposition rate for the first 200 s. (b) Steady-state polymer thickness.

etching. Etching simulations were conducted using the FC gas mixture for the 1200 W ICP. Blanket etching was simulated using a small (18 nm × 18 nm) unpatterned initial mesh. The mesh resolution (for all simulations presented here) is $\Delta x = 0.3$ nm, resulting in a 60 × 60 mesh.

The continuous etch rate, calculated as the change in height of the top solid surface (averaged over the computational domain) with respect to time, is shown in Fig. 4(a). This etch rate is negative (indicating net polymer deposition) for $V_{RF} \leq 20$ V for all materials. As V_{RF} is increased and the IED extends to higher energies, the plasma activation of the polymer becomes less efficient, reducing the polymer deposition rate and favoring thinner polymer layers. Polymer sputtering also increases with increasing ion energy, but at these energies still contributes little of the polymer loss mechanism. As ion energies and implant ranges increase with increasing V_{RF}, ions begin interacting more strongly with the etch front at the interface between the polymer and the underlying material. When etching begins, the SiO$_2$ consumes more polymer than Si$_3$N$_4$ or bare silicon due to the larger number of C–O bonds in the selvedge, which

produces a thinner layer of polymer on the SiO_2 than Si_3N_4 or Si for $V_{RF} > 20$ V, as shown in Fig. 4(b). This difference in polymer thickness results in selective etching of SiO_2 over Si_3N_4 and Si. These general trends have been experimentally observed for similar etching conditions.[6] The larger etch rate for Si_3N_4 above $V_{RF} = 80$ compared to Si in spite of the thicker polymer layer is likely a result of the lower threshold for chemically sputtering the $SiNC_xF_y$(s) complex than physically sputtering the Si.

Attempting continuous etching using the FC gas mixture with 300 W ICP power resulted in net deposition for $V_{RF} \leq$ 120 V. The increased polymer deposition is due to the lower $F/CF_{(2)}$ ratio for the lower power deposition. Since the total flux of polymerizing $CF_{(2)}$ radicals to the surface is larger for the 1200 W plasma, the polymer loss term in Eq. (1) is being dominated by fluorine etching under these conditions. While all biases (up 120 V) resulted in net deposition, the deposition rate decreased slightly with increasing ion energy due to less polymer activation at higher energies. At higher ion energies, where polymer sputtering by ions becomes a significant loss mechanism, these polymerizing fluxes may result in continuous etching conditions, but such energies are not of interest for ALE applications.

V. ALE BLANKET ETCHING

Using the ALE alternate pulsing scheme allows for more control of the passivation conditions over a wider range of operating conditions. Simulations of ALE of SiO_2 were conducted using the FC gas mixture for the passivation phase and impure argon for the ion bombardment. The passivation phase was 300 W ICP power and 0 V RF bias. These operating conditions were chosen because the resulting plasmas are highly polymerizing (due to the low $F/CF_{(2)}$ ratio described above), producing little continuous etching. In continuous etching, these fluxes would result in a rapid etch stop. However, in ALE, such conditions during the passivation phase can minimize deleterious continuous etching pathways. During this phase, the floating plasma potential results in an average ion energy of 14 eV incident on the wafer, as shown in Fig. 3(b), in spite there being no applied RF bias voltage. This energy is marginally larger than threshold energies of etching, technically placing the ion energies within the ALE window. In spite of being within the ALE window, these low energy ions can only etch exposed surface sites. Even thin polymer overlayers result in negligible etching during the passivation phase due to the inability of the 14 eV ions to penetrate the passivation, resulting in low rates of nonideal continuous etching during the passivation phase.

The ion bombardment phase was conducted with 600 W ICP power and 45 V RF bias in impure argon gas. The plasma conditions for the etching step were chosen to have commensurate ion fluxes to the substrate. To a good approximation, the scaling of the etching step to other reactors requires keeping the IED and ion fluence (time integrated flux) to the substrate constant. The ion energies during this phase are well contained in the ALE window. However, the presence of passivating radical species during this phase

(due to the C_4F_8 contamination) does result in some nonideal continuous etching at a rate of 0.5 nm/min.

Before modeling the complete ALE cycle for SiO_2 using realistic fluxes, ideal ALE was investigated. The fluxes and IEAD from the HPEM were used for the passivation phase. However, fluorocarbon radical fluxes were removed during the ion bombardment phase, leaving only fluxes of Ar^+ ions. With this modification, little continuous etching was produced during either the ion bombardment or passivation phases.

These ideal ALE conditions were used to perform simulations of SiO_2 blanket etching with passivation times, T_p, ranging from 50 ms to 35 s for three ion bombardment times ($T_i = 10$, 20, and 30 s). Periodic etching behavior occurs for all conditions, but not all conditions resulted in steady-state pulse-periodic etching. For example, the heights of the topmost layer of material (including polymer) are shown in Fig. 5(a). Etching with $T_i = 30$ s and $T_p = 7$ s resulted in a pulsed steady-state etching condition. With each FC plasma pulse, 0.8 nm of polymer was deposited, shown by the increase in height. With each argon plasma pulse, the
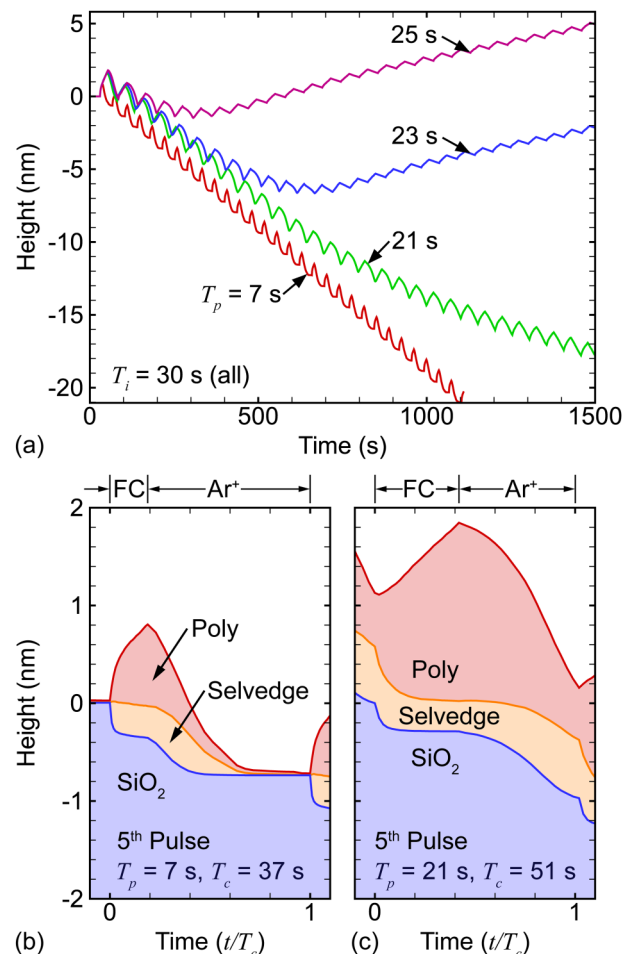

Fig. 5. Properties of SiO_2 ALE. (a) Change in total height (including polymer) as a function of time with $T_i = 30$ s for polymerization times of $T_p = 7$, 21, 23, and 25 s. Height of individual material layers during the fifth ALE pulse for (b) $T_p = 7$ s and (c) $T_p = 21$ s. The total ALE cycle time, T_c, is in each frame.

polymer was essentially fully removed, resulting in etching of 0.7 nm of SiO_2, shown by the decrease in height. Since the polymer deposition phase is not inherently self-limited, larger values of T_p result in a thicker polymer layer at the end of the passivation phase. For values of $T_p = 21$, 23, and 25 s, the polymer layer becomes too thick to entirely clear during the ion bombardment phase, eventually terminating the etching process and resulting in net deposition per cycle. This critical thickness is approximately the ion penetration depth, slightly more than 1 nm for these conditions. For the longer passivation times which have net deposition in the steady state, there is initially net etching which occurs before the polymer thickness increases above the critical thickness. The transition between net etching (pulse-periodic decrease in height) and net deposition (pulse-periodic increase in height) occurs at earlier times as T_p increases.

The surface kinetics of SiO_2 ALE, shown in Figs. 5(b) and 5(c), indicate two processes which erode the SiO_2. The first process results from the conversion of the base SiO_2 material to the selvedge material by exposure to $CF_{(2)}$ fluxes during the passivation phase. Since each SiO_2 surface site can only be converted once, this process is self-limited in the absence of energetic ion bombardment. After converting the surface to the selvedge material, further $CF_{(2)}$ fluxes result in polymer deposition on top of the selvedge layer, continuously increasing the total overlayer thickness. When a significant portion of the surface is bare SiO_2 at the beginning of the passivation phase [as is the case for $T_p = 7$ s, shown in Fig. 5(b)], there are two distinct polymer deposition rates. The initial rate is higher than later in the deposition phase due to the higher sticking coefficient of $CF_{(2)}$ on SiO_2 than other inactivated polymer species. Once the entire surface is covered with polymer, the polymer deposition rate decreases due to this lower sticking coefficient. Kaler *et al.* have also observed this effect and proposed that it may be utilized to produce pseudo-self-limiting behavior.[51]

The second process which results in the erosion of SiO_2 occurs during the ion bombardment phase. This erosion occurs as SiO_2 is converted to selvedge species by mixing with polymer when activated by ions penetrating through the polymer capping layer. Since all of the overlying polymer must be consumed during the ion bombardment phase in order for ALE to reach a pulse-periodic steady state, the amount of etching which occurs through this reaction channel is proportional to the initial polymer thickness. This results in an EPC which depends on polymer thickness, which in turn depends on T_p. Once all of the polymer is consumed, this erosion of SiO_2 terminates and the etch rate returns to zero. If T_p is sufficiently long with low ion energies, the greater thickness of polymer is not completely consumed during the ion bombardment phase [Fig. 5(c)]. The self-limited nature of the ion bombardment phase is then not exercised, and some of the benefits of ALE may not be as pronounced as a result.

With thinner polymer layers [Fig. 5(b)], the selvedge layer is eroded during the ion bombardment phase by ion activated processes such as chemical sputtering. This results in complete removal of the selvedge species from the surface

during ion bombardment as the polymer thickness goes to zero. When the polymer overlayer thickness is larger [Fig. 5(c)], the situation is different. In this case, the thickness of the selvedge layer increases during the ion bombardment phase due to ion mixing of the dielectric/polymer interface, but the distribution of selvedge species also evolves throughout this phase. The lack of fluorine radicals during the argon ion bombardment phase results in an abundance of SiF_x species in the selvedge layer, as one of the dominant etching pathways for this species (as depicted in Fig. 2) has been removed. At the beginning of the next passivation phase, the SiF_x selvedge species are rapidly consumed by the abundant fluorine radicals diffusing through the polymer, producing a brief period of selvage layer erosion during this phase, as visible in Fig. 5(c).

The pulse-periodic steady-state EPCs for different ion bombardment times, T_i, as a function of passivation time, T_p, are shown in Fig. 6. Using ideal SiO_2 ALE conditions, shown as dotted lines in Fig. 6(a), there is a wide range of passivation times which produce net etching. The EPCs shown here are measured after the system has reached a
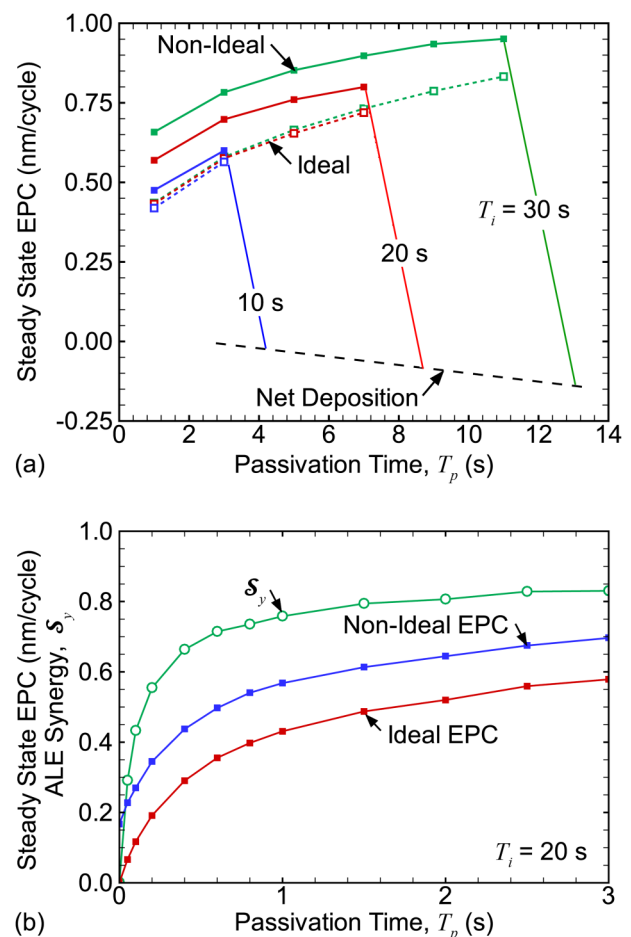

FIG. 6. Comparison of nonideal and ideal SiO_2 ALE properties. (a) Pulse-periodic steady-state EPC as a function of T_p, for $T_i = 10$, 20, and 30 s for ideal (dotted lines) and nonideal (solid lines) reactive fluxes. The diagonal lines indicate a transition from net etching to net deposition. (b) ALE synergy and steady state EPC for small values of T_p with $T_i = 20$ s. Values are shown for ideal and nonideal fluxes.

pulse-periodic steady state. Only conditions that completely clear the polymer from the surface during ion bombardment will have a positive EPC in the steady state. Conditions which do not completely clear the polymer will eventually transition to a net deposition condition in the steady state. For each T_i, there is a T_p above which pulse-periodic ALE cannot be achieved—that is, net deposition occurs in the steady state. This critical value of T_p increases with increasing T_i and represents the thickest polymer deposit which can be removed during the bombardment period. For passivation times longer than the critical T_p, the system produces net polymer deposition during each step. With the ion bombardment conditions being ideal, the EPC has little dependence on T_i for small values of T_p. That is, if there is no additional continuous etching due to $CF_{(2)}$ fluxes, the entire polymer layer will be utilized in etching if T_i is long enough (and T_p is less than the critical value). Despite the ideal conditions, there remains a dependence of EPC on T_p, increasing from 0.4 nm/cycle at $T_p = 1$ s to 0.8 nm/cycle at $T_p = 11$ s.

Similar simulations were conducted using the actual fluxes from the HPEM, representing realistic, nonideal ALE conditions. Under these conditions, the steady-state EPC of SiO₂, shown as solid lines in Fig. 6(a), has significant dependence on T_i, particularly at low values of T_p. There is a slightly reduced dependence on T_p, with the nonideal and ideal results converging, as T_p increases. The dependence of EPC on T_i is due to the nonideal etching occurring during the ion bombardment phase due to the fluorocarbon contamination in the chamber producing $CF_{(2)}$ fluxes. After the polymer deposited during the passivation phase is removed, thereby exposing the underlying SiO₂, the small flux of $CF_{(2)}$ due to contaminating C_4F_8 enables continuous etching during the ion bombardment phase. For example, Gasvoda *et al.* observed continuous etching during ALE of SiO₂ during the ion bombardment step, a process attributed to F-containing radicals coming from the reactor walls.[47]

The reduced dependence of EPC on T_p with nonideal conditions is a result of the polymer overlayer masking some of the nonideal etching for longer T_p. With longer T_p, the polymer overlayer persists for a larger portion of the ion bombardment phase. This effect results in the EPC for ideal and nonideal conditions converging as T_p increases, implying a larger portion of the total EPC is a result of the synergistic relationship between the two half-reactions as opposed to continuous etching. The trends for EPC with nonideal fluxes have the same saturating behavior as the ideal conditions, where above a critical value of T_p the steady-state etching stops and the system transitions to net deposition. The critical values of T_p are similar for ideal and nonideal conditions, within the resolution of this study ($\Delta T_p = 2$ s). This indicates that continuous etching does not significantly affect this process.

Evaluating the ALE quality for this process is more complex than halogen based ALE systems which leverage well defined self-limited processes. *ALE synergy* ($\mathcal{S}_y$) has been proposed as a metric for ALE processes.[3] The ALE synergy is the fraction of total etching which occurs due to

the synergy between the two half-reactions, as opposed to continuous etching during one phase or the other. For this metric to reach unity, etching cannot independently occur during either of the half-reaction processes. Only by cycling between the two half-reactions does etching occur. With halogen etching systems, it is possible to estimate $\mathcal{S}_y$ by measuring the etch rate of each half-reaction separately and evaluating $\mathcal{S}_y$ as

$$\mathcal{S}_y = \frac{EPC - (\alpha + \beta)}{EPC}, \tag{35}$$

where α and β are the continuous etch rates in during the passivation and ion bombardment phases multiplied by T_p and T_i, respectively. This method works well for ALE in halogen plasmas, where passivation layers are not much thicker than one monolayer. In fluorocarbon plasma ALE processes, this method for estimating $\mathcal{S}_y$ does not apply. Under the conditions discussed here, for instance, the ion bombardment phase has a continuous etch rate of 0.5 nm/min on SiO₂ due to the C_4F_8 impurity. The fluorocarbon fluxes from the plasma have a larger probability of sticking to bare SiO₂ than on a polymer surface. Therefore, when the surface is fully covered with polymer, the continuous etch rate would be less than on a bare SiO₂ surface. As the SiO₂ surface transitions from polymer covered to bare during each ALE pulse, it is difficult to directly evaluate β.

Given these difficulties, synergy will be estimated by comparing the nonideal EPC directly to the EPC obtained with idealized ALE fluxes. Synergy is then calculated as

$$\mathcal{S}_y = \frac{EPC_i}{EPC}, \tag{36}$$

where EPC_i refers to ideal conditions. The ALE synergy, calculated using Eq. (36), is shown in Fig. 6(b) using the steady-state EPC for ideal and nonideal etching for $T_p < 3$ s. The ion bombardment time is $T_i = 20$ s. The contribution of nonideal etching to EPC is fairly constant in this range. As the EPC decreases with smaller T_p, the nearly constant contribution by continuous etching becomes a larger fraction of the total which then reduces $\mathcal{S}_y$. At $T_p = 0$ s, etching can only occur due to the nonideal process during ion bombardment and so the etch rate for ideal etching is zero. The nonideal conditions produce etching of 0.16 nm/cycle, resulting in $\mathcal{S}_y = 0$. Synergy increases rapidly as T_p increases until reaching 0.8 at $T_p = 1.5$ s. After that point, $\mathcal{S}_y$ increases slowly to a value of 0.9 at $T_p = 7$ s. For larger values of T_p, the system transitions to net deposition in the pulse-periodic steady state.

In principle, the ALE of Si₃N₄ should follow the same trends as the ALE of SiO₂. In our mechanism, the distinguishing factor between fluorocarbon plasma etching of Si₃N₄ compared to SiO₂ is that etching of Si₃N₄ consumes less polymer than SiO₂. Due to this lower rate of polymer consumption, for the same reactive fluxes from the plasma, only values of $T_p < 1$ s resulted in pulse-periodic steady-state etching of Si₃N₄. This narrower window for ALE of Si₃N₄

suggests that there is a correspondingly large window in T_p where the selectivity to SiO$_2$ over nitride is large in the steady state. For T_p large enough to enter the net deposition regime, both materials perform identically.

While ALE may offer the possibility of high etch selectivity of SiO$_2$ over Si$_3$N$_4$ in the steady state, this selectivity is based on the buildup of polymer to levels that terminate etching of Si$_3$N$_4$, a sequence that requires several pulses to occur. Before the polymer layers become thick enough to enable selectivity, there is a transient period where the selectivity is less than the steady-state value. This transient period may result in significant etching of masking materials such as Si$_3$N$_4$ before reaching the steady state, which may be a limiting factor in some applications. For example, the heights of ALE etching SiO$_2$ and Si$_3$N$_4$ are shown in Fig. 7(a) for $T_i = 30$ s and $T_p = 5$ s. These conditions produce a pulse-periodic steady-state etching for SiO$_2$, however, significant etching of Si$_3$N$_4$ stops after approximately 15 cycles. For SiO$_2$ ALE, the polymer overlayer is nearly completely removed by the end of each cycle, as shown in Fig. 7(b). During the first few cycles of ALE of Si$_3$N$_4$, a residual layer

of polymer remains at the end of each cycle. This overlayer increases in thickness cycle to cycle, shown in Fig. 7(c), which reduces the EPC of the Si$_3$N$_4$. In spite of the fairly thick overlayer, the Si$_3$N$_4$ continues to etch with each cycle until the overlayer grows to about 2 nm, at which point Si$_3$N$_4$ etching essentially stops while the polymer layer continues to thicken.

While the thickness of the overlayer provides insights to the pulse-periodic characteristics of the surface kinetics, the distribution of selvedge species at the interface better reflects the kinetics of the surface reactions. The thickness of polymer and the selvedge species is shown in Fig. 8 as a function of time for ALE of SiO$_2$ and Si$_3$N$_4$ for $T_i = 30$ s and $T_p = 5$ s (same conditions as in Fig. 7).

For ALE of SiO$_2$, there are three selvedge species, SiO$_2$C$_x$F$_{y(s)}$, SiOC$_x$F$_{y(s)}$, and SiF$_{x(s)}$. At the beginning of the passivation phase, the surface is predominantly bare SiO$_2$. When exposed to passivating radicals, the SiO$_2$ surface is rapidly converted to SiO$_2$C$_x$F$_{y(s)}$, as shown in Fig. 8(a). A small fraction of these SiO$_2$C$_x$F$_{y(s)}$ sites begin to be converted to SiOC$_x$F$_{y(s)}$ during passivation due to some small fraction of above threshold ions. Since the probability of
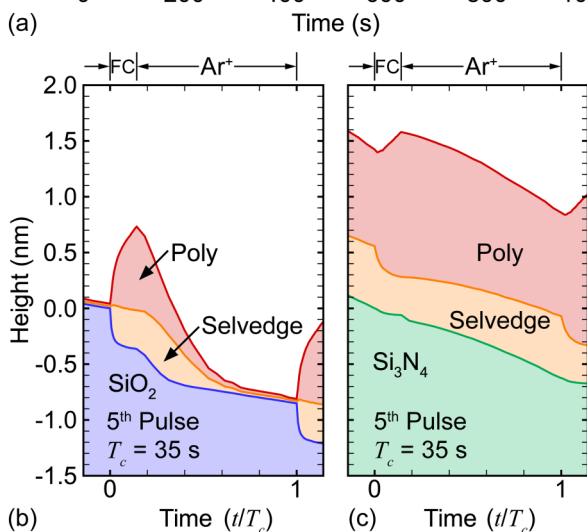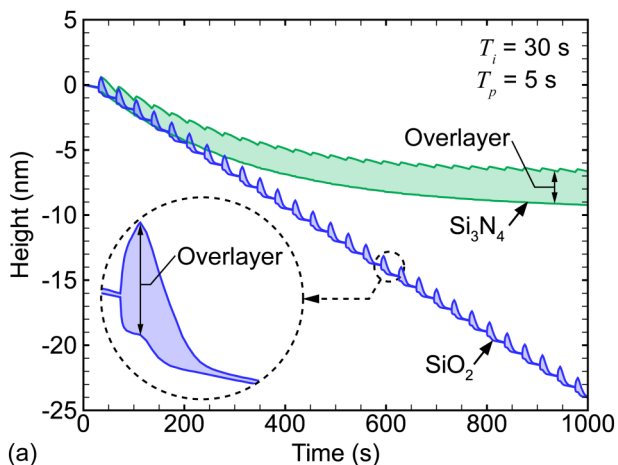

FIG. 7. ALE of SiO$_2$ and Si$_3$N$_4$ using nonideal fluxes. (a) Change in total height (including polymer) as a function of time for SiO$_2$ and Si$_3$N$_4$. The shaded regions represent the overlayer thickness comprised of both the selvedge and polymer layers. Height of individual material layers during the fifth ALE pulse for ALE of (b) SiO$_2$ and (c) Si$_3$N$_4$.
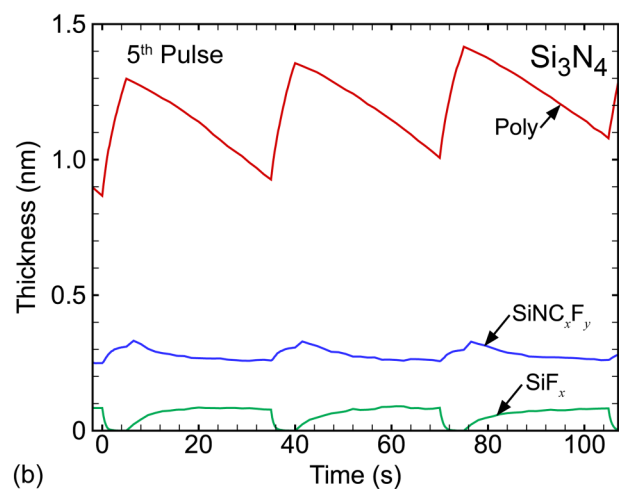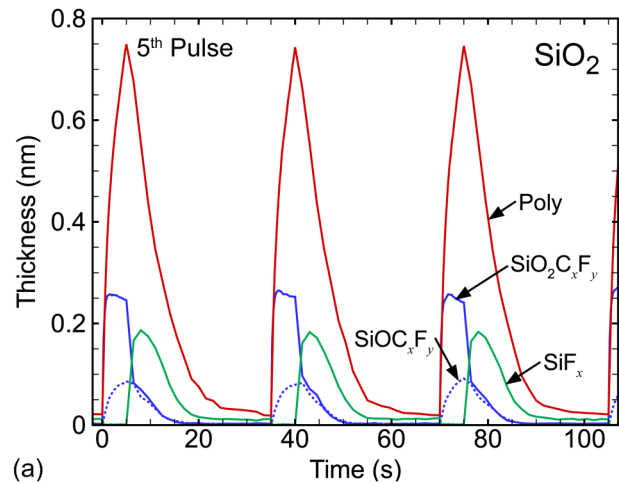

FIG. 8. Equivalent thickness of each overlayer species as a function of time during three ALE cycles ($t = 0$ is the start of the fifth cycle) for (a) SiO$_2$ and (b) Si$_3$N$_4$.

deoxygenating the SiOC$_x$F$_{y(s)}$ site is similar to the SiO$_2$C$_x$F$_{y(s)}$ site, it is likely that some of the SiOC$_x$F$_{y(s)}$ is also being converted to SiF$_{x(s)}$, but this species is rapidly consumed by the abundant fluorine radicals in the CF plasma. This is the dominant pathway of continuous etching during the passivation phase. However, this continuous etching is quite slow due to the average ion energy being below threshold for the two deoxygenation reactions after implanting through the overlayer.

During the ion bombardment phase, the SiO$_z$C$_x$F$_y$ species are rapidly converted to SiF$_{x(s)}$. However, since the flux of fluorine radicals is low during this phase, SiF$_{x(s)}$ is dominantly removed by sputtering as opposed to thermal etching. The polymer thickness grows during the passivation phase and is rapidly removed during the ion bombardment phase. The amount of polymer which is removed during ion bombardment is large because each deoxygenation reaction from the SiO$_2$ also removes a carbon atom polymer, represented in the model as removing a polymer site. With moderate ion bombardment times, the polymer becomes thin enough that the SiF$_{x(s)}$ species can be fully removed from the surface by sputtering.

The surface reactions are qualitatively different on Si$_3$N$_4$ compared to SiO$_2$. The Si$_3$N$_4$ etching mechanism only includes two selvedge species, SiNC$_x$F$_{y(s)}$ and SiF$_{x(s)}$. During ion bombardment, some of the SiNC$_x$F$_{y(s)}$ is converted to SiF$_{x(s)}$, as shown in Fig. 8(b) starting with the fifth ALE cycle. This process does not remove as much polymer as converting SiO$_2$C$_x$F$_{y(s)}$ to SiF$_{x(s)}$, so conditions which produce pulse-periodic steady-state ALE on SiO$_2$ do not necessarily completely clear the polymer on Si$_3$N$_4$. With this thicker polymer layer on Si$_3$N$_4$, the ion penetration depth during the ion bombardment phase may be comparable to or smaller than the polymer thickness. This results in ions reaching the etch front having low average energy (or not reaching the etch front) which precludes sputtering of the SiF$_{x(s)}$. During the passivation phase, the abundance of fluorine radicals rapidly etches the SiF$_{x(s)}$ surface species, providing additional etching during this phase. The result is that etching is nearly continuous for Si$_3$N$_4$, as shown in Fig. 7(c), in spite of the modulation of polymer thickness during the ALE cycle. The total polymer thickness continues to increase with each pulse, as shown in Fig. 8(b). This process of accumulating polymer with each pulse continues from pulse to pulse until the polymer thickness is large enough to produce an etch stop on Si$_3$N$_4$ [Fig. 7(a)].

The total changes in height of the substrate material for SiO$_2$ (ΔH_O) and Si$_3$N$_4$ (ΔH_N) after 15 pulses as a function of passivation time for different T_i are shown in Fig. 9. The value of ΔH indicates the removal of substrate material (SiO$_2$ or Si$_3$N$_4$) and is therefore always positive. (That is, the thickness of SiO$_2$ never increases during etching.) These results demonstrate the transient etching effect in Si$_3$N$_4$. For short T_p, the polymer deposited on the Si$_3$N$_4$ during each ALE cycle is small, resulting in a longer period of transient etching before polymer buildup terminates etching. The result is that low values of T_p result in larger ΔH for Si$_3$N$_4$ than SiO$_2$. As T_p increases, the ΔH for SiO$_2$ increases (more
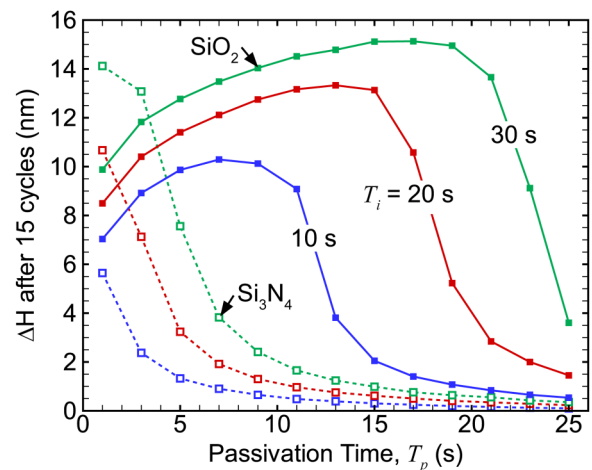

FIG. 9. Total change in height (ΔH) of the surface of SiO$_2$ or Si$_3$N$_4$ (not including overlayer) after 15 ALE cycles as a function of passivation time (T_p) for ion bombardment times (T_i) of 10, 20, and 30 s. SiO$_2$ ALE is shown as solid lines and Si$_3$N$_4$ as dotted lines.

net etching) due to the thicker resulting polymer layer fueling the etch longer during the ion bombardment phase—polymer that the SiO$_2$ mechanism is able to consume. This increase in ΔH with increasing T_p should continue as long as ions are able to penetrate through the polymer to reach the selvedge layer. With sufficiently long T_p, the polymer layer is too thick for significant ion penetration and etching cannot be supported. With Si$_3$N$_4$, ΔH monotonically decreases as T_p increases due to the shorter transient etching period associated with longer passivation times. For each T_i, there is a transition from steady-state etching conditions at low T_p to steady-state net deposition conditions at higher T_p. This transition occurs at larger T_p for longer T_i. The metric ΔH shows a measurable change in height for most of these conditions. However, etching may have completely ended for either or both SiO$_2$ and Si$_3$N$_4$ by the end of 15 pulses, which is not captured in this metric alone.

Selectivity for etching SiO$_2$ compared to Si$_3$N$_4$, defined as $\Delta H_O/\Delta H_N$, after 15 cycles is shown in Fig. 10(a). The results indicate that there is a trend of increasing maximum selectivity with increasing T_i. The T_p which produces the maximum selectivity also increases with T_i. For each T_i investigated, the peak selectivity occurs with a T_p that would not produce continuous pulse-periodic etching in the steady state. These trends indicate that conditions which do not produce a steady-state, pulse-periodic ALE may be useful for increasing selectivity in short etches, or when used as a preetch followed by conditions which would transition back into a pulse-periodic steady-state etch condition.

Transient etching plays an important role in the selectivity of SiO$_2$ compared to Si$_3$N$_4$ in a fluorocarbon plasma ALE process. As a result, the number of pulses required to complete the etch can change the resulting selectivity. For example, selectivity is shown in Fig. 10(b) as a function of T_p for $T_i = 20$ s. Fewer etch cycles result in decreased maximum selectivity for a given T_i. This occurs because the Si$_3$N$_4$ removal occurs mostly in the first 3–5 cycles for these conditions, resulting in a constant etch contribution for 5, 10,
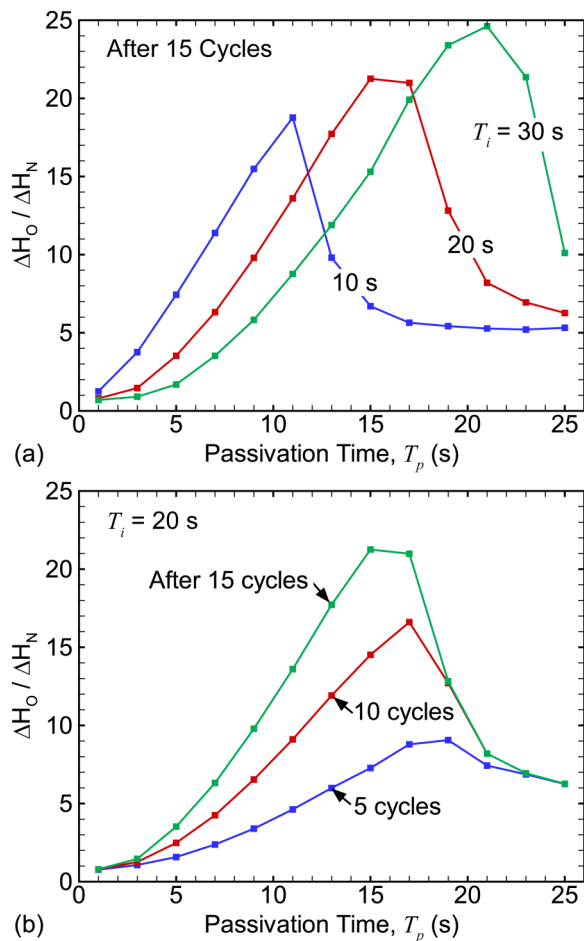
(a)

(b)

FIG. 10. Selectivity of ALE of SiO_2 over Si_3N_4. (a) Selectivity after 15 cycles as a function of passivation time (T_p) for ion bombardment times (T_i) of 10, 20, and 30 s. (b) Selectivity as a function of T_p for three different etch durations (5, 10, and 15 cycles) using $T_i = 20$ s.

and 15 cycles. The removal of SiO_2 still scales linearly with the number of cycles in this range. Accordingly, the constant ΔH_N results in the peak selectivity decreasing from 21 after 15 cycles to only 9 after 5 cycles. Depending on the film thickness to be removed, the transient etching behavior may be a limiting factor in process development.

VI. ALE FEATURE ETCHING

To demonstrate the influence of transient etching processes in ALE of SiO_2, simulations were performed of SAC geometry, shown in Fig. 11. In this plasma etching process, SiO_2 is removed from a high aspect ratio trench between Si_3N_4 features. The initial geometry is shown in Fig. 11(a). A small aspect ratio is used here to emphasize the selectivity aspects of the etch. The gap between gate features is 14 nm, and the computational domain is 78 nm (x) × 6 nm (y) × 187.5 nm (z). With a mesh resolution of $\Delta x = 0.3$ nm, the mesh contains 3.25×10^6 computational cells. Feature profiles for etching using a continuous process with RF biases of 40 V and 100 V are shown in Figs. 11(b) and 11(c). Continuous etching processes using similar conditions to those of ALE have difficulty etching this feature. Using the FC gas mixture
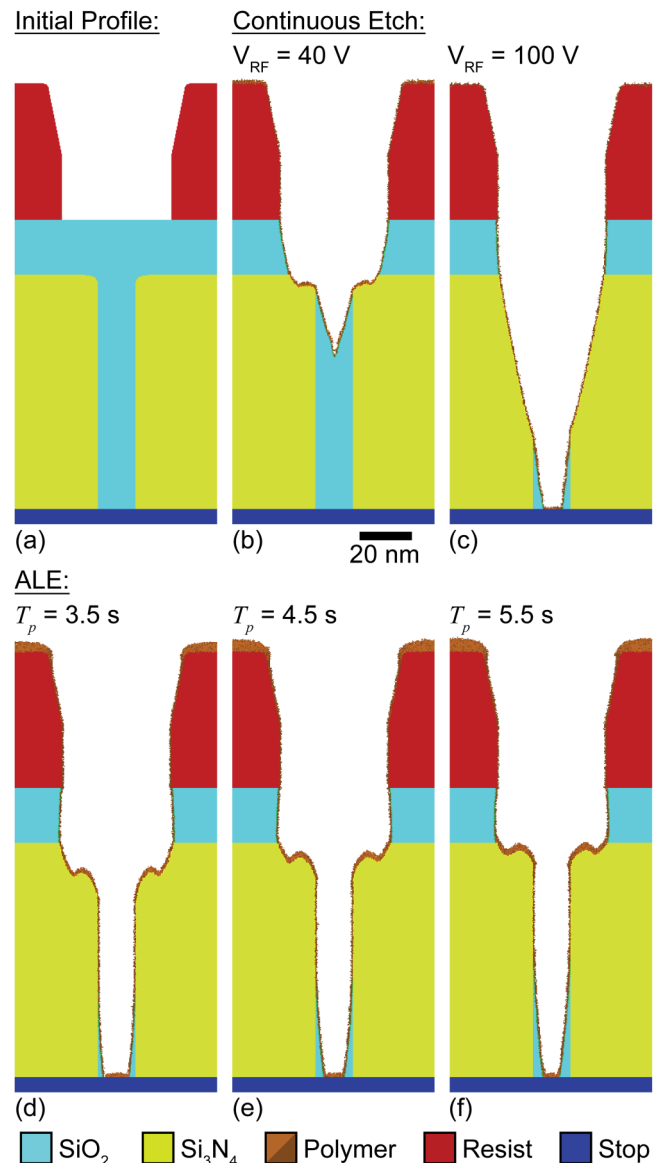

FIG. 11. Self-aligned contact etch profiles for continuous etching and ALE. (a) Initial profile. Continuous etch using the FC gas mixture with 1200 W ICP power for (b) $V_{RF} = 40$ V and (c) $V_{RF} = 100$ V. ALE profiles after 165 cycles using $T_i = 20$ s and $T_p = $ (d) 3.5 s, (e) 4.5 s, and (f) 5.5 s.

with $V_{RF} = 40$ V results in high selectivity of SiO_2 over Si_3N_4 during continuous etching, as shown in Fig. 4(a). Applying these conditions to the SAC geometry does result in little etching of the Si_3N_4, however, the tapering in the trench quickly leads to an etch stop in which the polymerization is too thick to allow etching to continue. The etch stop can be avoided by applying a larger bias of $V_{RF} = 100$ V. Using these conditions, the selectivity for SiO_2 significantly decreases, and the Si_3N_4 shoulders are eroded before the etch reaches the contact point at the bottom of the feature. These plasma conditions were not specifically optimized for this particular etch application. It is likely that other plasma etch conditions will perform better in this application.

ALE enables more control over the polymerization and selectivity of this process compared to continuous etching. Plasma conditions which could not complete the SAC etch

using continuous etching prove to be effective for ALE. Etch profiles are shown in Figs. 11(d)–11(f) using ALE with passivation times of $T_p = 3.5$, 4.5, and 5.5 s. The ion bombardment time was 20 s with the same ion energy distribution as previously used in blanket etching ($V_{RF} = 45$ V). The tapering of the feature is measured as *critical dimension (CD) loss*, which is the change in width of the trench between the Si$_3$N$_4$ from the top to a point 90% of the way down the feature, measured in nm. This CD loss is a measure of how much SiO$_2$ remains in the SAC feature near the bottom contact point. The width of the actual contact patch is not used to calculate CD loss here because that dimension is affected by the properties of the etch stop material, which is not calibrated in this case. The Si$_3$N$_4$ *shoulder loss* in nm is measured from the initial Si$_3$N$_4$ surface to the etched surface after the SAC feature has been cleared. The CD loss and shoulder loss are shown in Fig. 12 as a function of T_p after 166 cycles. The results indicate two trends—increasing T_p results in a decreased shoulder loss while producing increased CD loss. The decrease in shoulder loss is a direct result of larger T_p having higher selectivity, as discussed for blanket etching. With the higher T_p, the polymer layer reaches an etch stop thickness on Si$_3$N$_4$ more quickly, resulting in less transient etching. Comparing the profiles in Figs. 11(d)–11(f), the polymer layer protecting the Si$_3$N$_4$ is thicker for larger T_p.

Critical dimension loss in the SAC feature is a multidimensional phenomenon, meaning that it cannot exist in a 1-d blanket etch scenario, and its root causes cannot be inferred from blanket results. While ALE can help obtain ideal, non-tapered, feature profiles,[57] the underlying fluorocarbon plasma etch process has a strong propensity for generating tapered features, as shown in Fig. 11(b). This taper results from particulars of the ion energy, polymerization on the sidewalls, the angular dependence of sputtering yield, and the redeposition of etch products within the feature.[58–61] The reason the feature taper persists in the ALE case is related to a low ion sputtering yield of SiO$_2$ for near-grazing ion impacts on the tapered walls. In the halogen plasma ALE of

silicon, the selvedge layer which is to be removed during ion bombardment is directly exposed to the plasma and to ion bombardment. Direct plasma exposure increases sputtering yield when compared to sputtering through a thick passivation layer, but the total yield is still low at grazing and near-grazing angles. As a result, a larger T_i/T_p ratio is needed to clear passivated surface sites on tapered sidewalls. This effect was previously observed using our model for Cl$_2$/Ar plasma ALE of silicon when clearing residual silicon from the tapered sidewalls between fins during gate etching.[62]

In fluorocarbon plasma ALE of SiO$_2$, sensitivity to the angular dependence of sputtering yield during the ion bombardment phase is exacerbated by polymer buildup on the walls. Ions striking the tapered sidewall at a near-grazing angle must penetrate the polymer layer to interact with the underlying selvedge layer. This is less likely at near-grazing incidence than normal incidence. First, the straight line path to the selvedge layer through the polymer is longer for near-grazing ions compared to normal ions. Second, even small-angle scattering as the ion implants through the polymer layer can result in a large portion of near-grazing impacts reemerging into the plasma. On the other hand, normal incidence ions would have to undergo >90° of total scattering before they could emerge from the polymer layer, making it much less likely to occur before interacting with the selvedge layer. These trends result in ions interacting with the selvedge layer being less likely with a polymer overlayer than without. The main source of polymer removal during the ion bombardment phase is consumption of the polymer layer by ions interacting with the selvedge layer. This depletion mechanism results in a polymer overlayer which is more difficult to remove from tapered sidewalls than horizontal surfaces and encourages tapering of the feature. From this perspective, larger T_p producing thicker polymer layers will result in a more tapered feature for a given T_i.

ALE will likely require longer processing times than continuous etching, and so it may be advantageous to integrate a continuous main etch with an ALE clean-up. As an example of this process, an integrated etch was simulated for an SAC feature with a thicker SiO$_2$ overlayer (110 nm) having a larger aspect ratio than the previous examples. The resulting profile is shown in Fig. 13. In this case, using only ALE would likely have a prohibitive cost due to the large number of cycles required to etch through the thick SiO$_2$ overlayer. Instead, much of the SiO$_2$ layer is removed using a continuous main etch using an Ar/C$_4$F$_8$/O$_2$ = 90/5/5 plasma with an RF bias of 60 V. Oxygen atoms, produced by electron impact with O$_2$ in the plasma, readily etch the CF$_x$ polymer resulting in a thin polymer and little or no selectivity of SiO$_2$ over the Si$_3$N$_4$ gate features. These conditions are unacceptable for etching the entire SAC geometry due to the lack of selectivity. Therefore, the main etch is stopped when the etch front reaches the depth of the Si$_3$N$_4$ features, and an ALE etch started to remove the SiO$_2$ between the Si$_3$N$_4$ features. The ALE conditions were $T_i = 20.0$ s and $T_p = 5.5$ s [which are the same conditions for the results shown in Fig. 11(f)]. Using the integrated process results in the ALE beginning from a tapered etch front. In spite of the difference in initial
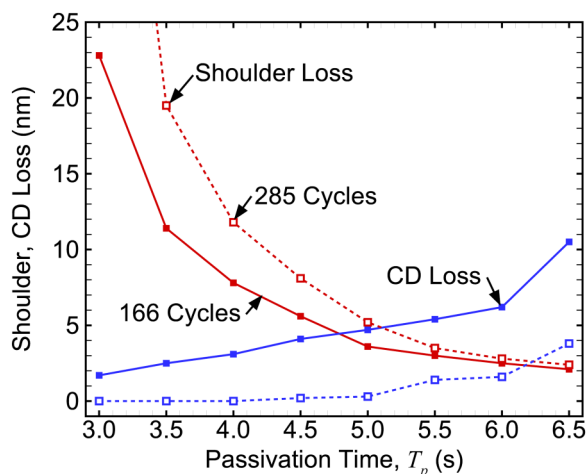

FIG. 12. Shoulder loss and CD loss as a function of passivation time for ALE of the SAC feature with $T_i = 20$ s.
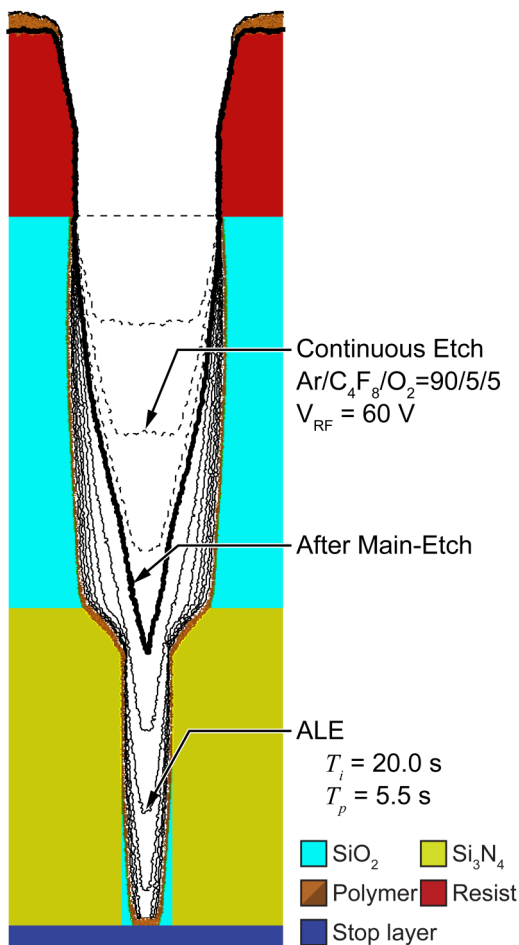
FIG. 13. Integrated etch of SAC feature with 110 nm SiO_2 overlayer. The dotted lines show etch front propagating during continuous main etch. The thick solid line represents the profile when the main etch is complete and ALE begins. The thinner lines represent the etch front evolution during ALE. The final profile is shown in color.

conditions compared to the small AR features, the resulting contact for the integrated process closely resembles the results for Fig. 11(f), including low shoulder and CD loss. These results indicate that it is possible to integrate ALE clean-up etches with continuous main etch conditions, enabling the use of ALE in applications where performing ALE exclusively would be difficult.

VII. ROLE OF POLYMER IN DIELECTRIC PLASMA ALE

The results of plasma ALE using FC gas mixtures for blanket and SAC features indicate that controlling polymer thickness is essential to the process. ALE offers an opportunity to control polymer thickness that is not available when using continuous plasma processing. Unfortunately, polymer deposition is not a fully self-limited process, making some of the benefits of ALE processing difficult to obtain. The selectivity, EPC, ALE synergy, and CD loss all depend on polymer thickness, which in turn depends on fluxes of polymerizing species, fluxes of polymer etching radicals, and fluxes of ions and ion energies (due to ion activation of the polymer layer and sputtering). This strong coupling of most or all of the important quality metrics for polymer thickness, combined with the lack of a truly self-limited polymer deposition reaction, results in several trade-offs that need to be made in ALE process design.

Running an ALE process in the thick polymer regime, close to where the system will transition to net deposition, can provide several benefits. As shown in Fig. 6(a), the EPC quasi-saturates at higher passivation times, indicating that in this regime the EPC is less dependent on polymer thickness. As T_p increases, the EPC for ideal and nonideal ALE fluxes converge. These trends indicate that the thick polymer regime has a higher ALE synergy by suppressing continuous etching during the ion bombardment phase. Having higher ALE synergy and lower dependence of EPC on polymer thickness implies that operating with these conditions would result in lower aspect ratio dependent etch rates (ARDE). Unfortunately, these benefits only occur at the edge of continuous etching conditions, where the polymer layer is only just removed during each ALE cycle. These conditions are, in some ways, an unstable steady-state condition. If conditions in the reactor change toward higher polymer deposition per cycle, either as a result of reactor wall seasoning or changing conditions with increasing aspect ratio in the feature, it is possible to rapidly transition to net deposition.

While many of the benefits of ALE seem to be optimized by operating in a thick polymer regime, etching of the SAC demonstrates that there is a tradeoff between selectivity and CD loss (tapering) for these conditions. The results shown in Fig. 12 indicate that CD loss increases with increasing polymerization time T_p up to 6.5 s. For $T_p \geq 7$ s, an etch stop occurred before reaching the bottom contact material due to excessive polymer buildup in a fully tapered feature. The blanket ALE results, shown in Fig. 6(a), indicate that steady-state etching can be achieved with $T_p = 7$ s for $T_i = 20$ s, slightly longer polymerization time than was possible in the high aspect ratio feature. The high aspect ratio feature may impose a more strict limit on polymer deposition before etch stop occurs compared to blanket etching.

Another consideration when evaluating the ALE of high aspect ratio features is over-etch. (Over-etch refers to the additional time that etching proceeds to clear the entire feature following any point in the feature reaching the etch stop bottom layer.) The results presented in Fig. 12 are for the same number of ALE cycles, which represent about a 10% over-etch for $T_p = 6.5$ s. Using the same number of cycles enabled a side-by-side comparison of the different conditions. If the over-etch is increased for each set of conditions, the CD loss can be reduced. In fact, if the over-etch is extended to 90% (285 cycles) the CD loss can be nearly eliminated without dramatically increasing the shoulder loss, shown as dotted lines in Fig. 12. For instance, at $T_p = 6$ s, the CD loss decreased from 6.2 to 1.6 nm, while the shoulder loss increased from 2.5 to 2.8 nm. The increase in over-etch has a larger effect on shoulder loss for smaller passivation times. For longer passivation times, the over-etch does not significantly increase shoulder loss because the majority of Si_3N_4 etching was during the short transient period at the

beginning of the etch. If evaluated during the last several cycles of the process when the over-etch actually occurs, the selectivity to SiO$_2$ would be essentially infinite.

VIII. CONCLUDING REMARKS

Atomic layer etching represents an opportunity to control polymer deposition during etching of SiO$_2$ in fluorocarbon plasmas, which in turn enables finer control over selectivity, etch rate, and profile propagation compared to continuous etching for comparable conditions. The results from our computational investigation indicate that ALE using cyclic pulses of a polymerizing C$_4$F$_8$ containing plasma, and an argon plasma for ion bombardment of the passivated surface, can result in stable pulse-periodic steady-state ALE of SiO$_2$. Being able to achieve this steady state is in part due to the consumption of polymer during the SiO$_2$ etch cycle, which can effectively clear the SiO$_2$ surface of polymer in spite the use of low energy nonreactive species for ion bombardment. For the same conditions, it is difficult to completely clear the polymer overlayer from Si$_3$N$_4$ surfaces during the ion bombardment phase, which eventually leads to polymer buildup and an etch stop. These conditions lead to effectively infinite selectivity of SiO$_2$ over Si$_3$N$_4$ for ALE in the pulse-periodic steady state.

Transient etching before the polymer overlay has fully developed has an important role in the ALE of SiO$_2$, and particularly in its selectivity over Si$_3$N$_4$. Conditions which will eventually lead to an etch stop on Si$_3$N$_4$ can also produce significant etching in the first several ALE cycles before the polymer overlayer is thick enough to prevent further etching. For many applications, including the SAC etch process discussed above, this initial transient etching of Si$_3$N$_4$ can be a limiting factor for the selectivity of SiO$_2$ over Si$_3$N$_4$. For etching of thinner films, for example, those requiring less than 10 ALE cycles, the limitations on the selectivity of the ALE scheme used here would be challenging to overcome. One possible remedy is predosing the passivation phase to achieve a thicker initial polymer layer to preserve the selectivity of SiO$_2$ over Si$_3$N$_4$ achievable in the pulse-periodic steady state.

ACKNOWLEDGMENTS

[1]K. J. Kanarik, T. Lill, E. A. Hudson, S. Sriraman, S. Tan, J. Marks, V. Vahedi, and R. A. Gottscho, J. Vac. Sci. Technol. A **33**, 20802 (2015).

[2]R. A. Gottscho, C. W. Jurgensen, and D. J. Vitkavage, J. Vac. Sci. Technol. B **10**, 2133 (1992).

[3]K. J. Kanarik *et al.*, J. Vac. Sci. Technol. A **35**, 5 (2017).

[4]D. Metzler, R. L. Bruce, S. Engelmann, E. A. Joseph, and G. S. Oehrlein, J. Vac. Sci. Technol. A **32**, 20603 (2014).

[5]T. E. F. M. Standaert, C. Hedlund, E. A. Joseph, G. S. Oehrlein, and T. J. Dalton, J. Vac. Sci. Technol. A **22**, 53 (2004).

[6]M. Schaepkens, T. E. F. M. Standaert, N. R. Rueger, P. G. M. Sebel, G. S. Oehrlein, and J. M. Cook, J. Vac. Sci. Technol. A **17**, 26 (1999).

[7]T. E. F. M. Standaert, M. Schaepkens, N. R. Rueger, P. G. M. Sebel, G. S. Oehrlein, and J. M. Cook, J. Vac. Sci. Technol. A **16**, 239 (1998).

[8]M. J. Barela, H. M. Anderson, and G. S. Oehrlein, J. Vac. Sci. Technol. A **23**, 408 (2005).

[9]C. Li, D. Metzler, C. S. Lai, E. A. Hudson, and G. S. Oehrlein, J. Vac. Sci. Technol. A **34**, 041307 (2016).

[10]T. Tatsumi, M. Matsui, M. Okigawa, and M. Sekine, J. Vac. Sci. Technol. B **18**, 1897 (2000).

[11]E. Gogolides, P. Vauvert, G. Kokkoris, G. Turban, and A. G. Boudouvis, J. Appl. Phys. **88**, 5570 (2000).

[12]S. Osher and J. A. Sethian, J. Comput. Phys. **79**, 12 (1988).

[13]O. Ertl and S. Selberherr, Microelectron. Eng. **87**, 20 (2010).

[14]T. Shimada, T. Yagisawa, and T. Makabe, Jpn. J. Appl. Phys. **45**, 8876 (2006).

[15]A. P. Mahorowala and H. H. Sawin, J. Vac. Sci. Technol. B **20**, 1064 (2002).

[16]W. Guo, B. Bai, and H. H. Sawin, J. Vac. Sci. Technol. A **27**, 388 (2009).

[17]W. Guo and H. H. Sawin, J. Vac. Sci. Technol. A **28**, 250 (2010).

[18]P. J. Stout, S. Rauf, A. Nagy, and P. L. G. Ventzek, J. Vac. Sci. Technol. B **24**, 1344 (2006).

[19]Y. Osano and K. Ono, Jpn. J. Appl. Phys. **44**, 8650 (2005).

[20]Y. Osano and K. Ono, J. Vac. Sci. Technol. B **26**, 1425 (2008).

[21]K. Ono, N. Nakazaki, H. Tsuda, Y. Takao, and K. Eriguchi, J. Phys. D Appl. Phys. **50**, 414001 (2017).

[22]S. Takagi, S. Onoue, K. Nishitani, T. Shinnmura, and Y. Shigesato, Jpn. J. Appl. Phys. **54**, 36501 (2015).

[23]S. Takagi *et al.*, Plasma Sources Sci. Technol. **12**, S64 (2003).

[24]N. Kuboi, T. Tatsumi, T. Kinoshita, T. Shigetoshi, M. Fukasawa, J. Komachi, and H. Ansai, J. Vac. Sci. Technol. A **33**, 061308 (2015).

[25]M. J. Kushner, J. Phys. D Appl. Phys. **42**, 194013 (2009).

[26]A. V. Vasenkov, X. Li, G. S. Oehrlein, and M. J. Kushner, J. Vac. Sci. Technol. A **22**, 511 (2004).

[27]Y. Zhang, C. Huard, S. Sriraman, J. Belen, A. Paterson, and M. J. Kushner, J. Vac. Sci. Technol. A **35**, 21303 (2017).

[28]M. Wang and M. J. Kushner, J. Vac. Sci. Technol. A **29**, 51306 (2011).

[29]T. J. Pricer, M. J. Kushner, and R. C. Alkire, J. Electrochem. Soc. **149**, C396 (2002).

[30]S. A. Islam, "Math Notes-Least Squares Plane," see http://www.sbg.bio.ic.ac.uk/~islam/plane.html.

[31]L. N. Trefethen and D. Bau, *Numerical Linear Algebra* (Society for Industrial and Applied Mathematics, Philadelphia, 1997).

[32]G. E. Farin and D. Hansford, *Practical Linear Algebra: A Geometry Toolbox* (CRC, Boca Raton, FL, 2013).

[33]H. D. Hagstrum, Phys. Rev. **122**, 83 (1961).

[34]W. Steckelmacher, Rep. Prog. Phys. **49**, 1083 (1986).

[35]F. Celestini and F. Mortessagne, Phys. Rev. E **77**, 21202 (2008).

[36]C. Steinbrüchel, Appl. Phys. Lett. **55**, 1960 (1989).

[37]J. P. Chang and H. H. Sawin, J. Vac. Sci. Technol. B **19**, 1319 (2001).

[38]N. R. Rueger, M. F. Doemling, M. Schaepkens, J. J. Beulens, T. E. F. M. Standaert, and G. S. Oehrlein, J. Vac. Sci. Technol. A **17**, 2492 (1999).

[39]R. A. Fisher and F. Yates, *Statistical Tables for Biological, Agricultural and Medical Research* (Oliver and Boyd, Edinburgh, 1949).

[40]J. F. Ziegler, M. D. Ziegler, and J. P. Biersack, Nucl. Instrum. Methods B **268**, 1818 (2010).

[41]C. T. Rettner, J. A. Barker, and D. S. Bethune, Phys. Rev. Lett. **67**, 2183 (1991).

[42]B. A. Helmer and D. B. Graves, J. Vac. Sci. Technol. A **16**, 3502 (1998).

[43]H. Ito, T. Kuwahara, K. Kawaguchi, Y. Higuchi, N. Ozawa, S. Samukawa, and M. Kubo, J. Phys. Chem. C **118**, 21580 (2014).

[44]S. Matteson, Appl. Phys. Lett. **39**, 288 (1981).

[45]N. Metropolis, A. W. Rosenbluth, M. N. Rosenbluth, A. H. Teller, and E. Teller, J. Chem. Phys. **21**, 1087 (1953).

[46]D. W. Bassett and P. R. Webber, Surf. Sci. **70**, 520 (1978).

[47]R. J. Gasvoda, A. W. van de Steeg, R. Bhowmick, E. A. Hudson, and S. Agarwal, ACS Appl. Mater. Infer. **9**, 31067 (2017).

[48]G. Cunge and J. P. Booth, J. Appl. Phys. **85**, 3952 (1999).

[49]H. Chae, S. A. Vitale, and H. H. Sawin, J. Vac. Sci. Technol. A **21**, 381 (2003).

[50]G. S. Oehrlein, Y. Zhang, D. Vender, and M. Haverlag, J. Vac. Sci. Technol. A **12**, 323 (1994).

[51]S. S. Kaler, Q. Lou, V. M. Donnelly, and D. J. Economou, J. Phys. D Appl. Phys. **50**, 234001 (2017).

⁵²Samuel B. Wainhaus, Eric A. Gislason, and L. Hanley, J. Am. Chem. Soc. **119**, 4001 (1997).

⁵³E. R. Fuoco and L. Hanley, J. Appl. Phys. **92**, 37 (2002).

⁵⁴A. Goodyear and M. Cooke, J. Vac. Sci. Technol. A **35**, 01A105 (2017).

⁵⁵M. Schaepkens, R. C. M. Bosch, T. E. F. M. Standaert, G. S. Oehrlein, and J. M. Cook, J. Vac. Sci. Technol. A **16**, 2099 (1998).

⁵⁶K. Miyata, M. Hori, and T. Goto, J. Vac. Sci. Technol. A **14**, 2083 (1996).

⁵⁷C. G. N. Lee, K. J. Kanarik, and R. A. Gottscho, J. Phys. D Appl. Phys. **47**, 273001 (2014).

⁵⁸M. Tuda and K. Ono, Jpn. J. Appl. Phys. **36**, 2482 (1997).

⁵⁹M. Tuda, K. Shintani, and H. Ootera, J. Vac. Sci. Technol. A **19**, 711 (2001).

⁶⁰T. Ohiwa, K. Horioka, T. Arikado, I. Hasegawa, and H. Okano, Jpn. J. Appl. Phys. **31**, 405 (1992).

⁶¹I. L. Berry, K. J. Kanarik, T. Lill, S. Tan, V. Vahedi, and R. A. Gottscho, J. Vac. Sci. Technol. A **36**, 01B105 (2018).

⁶²C. M. Huard, Y. Zhang, S. Sriraman, A. Paterson, K. J. Kanarik, and M. J. Kushner, J. Vac. Sci. Technol. A **35**, 31306 (2017).